JGR Earth Surface

RESEARCH ARTICLE
10.1029/2021JF006152

Modeling the Morphodynamic Response of Estuarine Intertidal Shoals to Sea-Level Rise

H. Elmilady[1,2,3], **M. van der Wegen**[1,2], **D. Roelvink**[1,2,3], **and A. van der Spek**[2,4]

[1]Department of Coastal and Urban Risk and Resilience, IHE Delft, Delft, The Netherlands, [2]Department of Applied Morphodynamics, Deltares, Delft, The Netherlands, [3]Faculty of Civil Engineering and Geosciences, TU Delft, Delft, The Netherlands, [4]Faculty of Geosciences, Utrecht University, Utrecht, The Netherlands

Key Points:

- Tidal currents are the main driver for the morphodynamic response of estuarine channel-shoal systems to sea-level rise (SLR)
- Intertidal shoals accrete under SLR with a lag that increases as SLR accelerates, eventually causing shoals to drown
- Wave action, increased sediment supply, and the presence of mud enhance the morphodynamic adaptation of intertidal shoals to SLR

Supporting Information:

Supporting Information may be found in the online version of this article.

Correspondence to:

H. Elmilady,
h.elmilady@un-ihe.org

Citation:

Elmilady, H., van der Wegen, M., Roelvink, D., & van der Spek, A. (2022). Modeling the morphodynamic response of estuarine intertidal shoals to sea-level rise. *Journal of Geophysical Research: Earth Surface*, *127*, e2021JF006152. https://doi.org/10.1029/2021JF006152

Received 6 MAR 2021
Accepted 3 DEC 2021

Abstract Intertidal shoals are key features of estuarine environments worldwide. Climate change poses questions regarding the sustainability of intertidal areas under sea-level rise (SLR). Our work investigates the SLR impact on the long-term morphological evolution of unvegetated intertidal sandy shoals in a constrained channel-shoal system. Utilizing a process-based model (Delft3D), we schematize a short tidal system in a rectangular (2.5 × 20 km) basin with a high-resolution grid. An initial, mildly sloping, bathymetry is subjected to constant semidiurnal tidal forcing, sediment supply, and small wind-generated waves modeled by SWAN. A positive morphodynamic feedback between hydrodynamics, sediment transport, and morphology causes the emergence of large-scale channel-shoal patterns. Over centuries, tide-residual sediment transport gradually decreases leading to a state of low morphological activity balanced by tides, waves, and sediment supply. Tidal currents are the main driver of the SLR morphodynamic adaptation. Wave action leads to wider and lower shoals but does not fundamentally change the long-term morphological evolution. SLR causes increased flood dominance which triggers sediment import into the system. Shoals accrete in response to SLR with a lag that increases as SLR accelerates, eventually causing intertidal shoals to drown. Seaward shoals near the open boundary sediment source have higher accretion rates compared to landward shoals. Similarly, on a shoal-scale, the highest accretion rates occur at the shoal edges bounding the sediment suppling channels. A larger sediment supply enhances the SLR adaptation. Waves help distribute sediment supplied from channels across shoals. Adding mud fractions leads to faster, more uniform, accretion and muddier shoals under SLR.

Plain Language Summary The intertidal zone is defined as the area between high and low water, where land meets the sea. Intertidal ecosystems have a high environmental and economic value. The currently observed and forecasted sea-level rise (SLR) rates raise questions on the fate of intertidal areas. While natural unconstrained systems could adapt to SLR by lateral expansion or landward migration, systems constrained by sea defenses or geology face a greater risk. Our research applies a model to investigate the impact of SLR on the century-time scale morphological evolution of unvegetated intertidal shoals in a constrained system. Model results show that shoals accrete under SLR. However, the accretion is lower than the SLR eventually leading to loss of intertidal shoal areas. Locations near a sediment source adapt better to SLR. Small wind-generated waves, increased sediment supply, as well as the presence of mud in the system enhance the morphodynamic adaptation to SLR. The knowledge developed in this study serves as a fundamental step toward understanding the potential impact of SLR on the sustainability of the valuable intertidal environment.

1. Introduction

The intertidal zone is a key component of many estuaries and tidal basins. It provides flood protection, erosion control (Narayan et al., 2017; Reed et al., 2018), has significant recreational and cultural value (Wilson et al., 2005), and includes valuable habitats for fish, benthic species, and birds (e.g., Galbraith et al., 2002; Lipcius et al., 2013).

Worldwide, intertidal areas are experiencing a notable decline due to anthropogenic impact and climate change (Airoldi & Beck, 2007; Murray et al., 2014, 2019; Song et al., 2020). Pressure sources include urbanization (Lai et al., 2015; MacKinnon et al., 2012), changes in riverine flows and sediment supply (Blum & Roberts, 2009; Jaffe et al., 2007), and sea-level rise (SLR; Lovelock et al., 2017; Passeri et al., 2015).

Ensuring the sustainability of soft-sediment intertidal environments (e.g., unvegetated intertidal shoals) requires an understanding of the processes governing their capacity for SLR adaptation. The global mean sea level (MSL)

has increased by about 20–25 cm since 1880, with about 9.5 cm since 1993 (NASA, 2020; Sweet et al., 2017). The current global SLR rate is about 3.3 mm/yr (NASA, 2020) which is unprecedented over the past 2 millennia (Kemp et al., 2011; Kopp et al., 2016). This rate is predicted to accelerate, although exact rates remain uncertain. SLR projections for the 21st-century range from about 0.3 to 2.7 m, depending on the potential rapid loss of the Antarctic ice sheet mass (Church et al., 2013; Le Bars et al., 2017; Miller et al., 2013; Sweet et al., 2017).

Channel-shoal systems form as a result of an instability of the morphodynamic system under tidal currents. This triggers a positive morphological feedback leading to the emergence of large-scale channel-shoal patterns when tide-residual transports converge over shoals enhancing their growth and diverge in the channels leading to their deepening (Coeveld et al., 2003; Schramkowski et al., 2002; Seminara & Tubino, 2001). Over decades to centuries, the residual transports gradients gradually diminish resulting in decreased morphological activity and stable patterns (e.g., Hibma, 2004; van der Wegen & Roelvink, 2008). Shoals can exist in a free form surrounded by deeper channels or in a fringing form connected to the land.

In addition to tidal currents, fine sediment (mud, $4 < D50 < 62.5$ μm, or very fine and fine sand, $62.5 < D50 < 250$ μm; Wentworth, 1922) supply is a key factor for tidal flat formation (e.g., Friedrichs, 2011; Reineck & Singh, 1980). Fine fractions are more effectively transported by tidal currents toward calmer shoal locations than coarser fractions which can resist the higher flow velocities in deeper channels. For example, sand dominates the Western Scheldt estuary and Wadden Sea (The Netherlands) with coarser sandy material present in channels than on the shoals, while mud dominates the low energy locations (Kuijper et al., 2004; Postma, 1957).

Relatively high wave impact at open coasts causes the formation of steep sandy beaches. Calmer wave conditions around sheltered locations in estuaries or tidal basins allow for the formation of intertidal shoals. However, relatively small waves can still play an important role in shaping the intertidal morphology (e.g., Allen & Duffy, 1998; Christie et al., 1999; Elmilady et al., 2020; Friedrichs & Aubrey, 1996; Janssen-Stelder, 2000; Roberts et al., 2000; van der Wegen et al., 2017). Measurements show that subsequent periods of lower and higher wave action cause cycles of shoal erosion and deposition, respectively (e.g., Fan et al., 2002; Houser & Hill, 2010; Janssen-Stelder, 2000; Kohsiek et al., 1988).

Observations and modeling studies suggest that, over decades to centuries, shoals evolve toward a state of decreased morphological activity (Elmilady et al., 2020; Friedrichs, 2011; Maan et al., 2018; Roberts et al., 2000; van der Wegen et al., 2017). Short-term forcing variations such as storm activity (de Vet, 2020; Elmilady et al., 2020; Q. Zhu et al., 2017) or seasonal changes (van der Wegen et al., 2019) result in morphological adaptation which, in most instances, recovers when normal forcing is restored. On the other hand, longer-term forcing variations can notably impact the intertidal morphology (e.g., de Vet et al., 2017; Jaffe et al., 2007).

SLR will impact the hydrodynamics of tidal systems including tidal current velocities, tidal asymmetry, and tidal range (Friedrichs et al., 1990; Jiang et al., 2020; Seiffert et al., 2014; Wachler et al., 2020). The anticipated impact depends on the basin geometry and bathymetry (Du et al., 2018; Friedrichs et al., 1990; Leuven et al., 2019). Changes in the tidal regime will influence residual sediment transports and the associated import/export trends and it will trigger a long-term morphological adaptation process (e.g., Dissanayake et al., 2009; van der Wegen, 2013).

Different modeling strategies are available to assess SLR impact on the morphodynamics of estuarine systems. Lodder et al. (2019) Rossington and Spearman (2009), Van Goor et al. (2003) and Wang et al. (2018) show the ability of low-resolution models based on empirical equilibrium relationships to reproduce historic decadal morphological development and predict SLR impact. Process-based, high-resolution modeling studies include real case studies with validated hindcasts followed by SLR forecasts (Elmilady et al., 2019; Ganju & Schoellhamer, 2010; van der Wegen et al., 2017; X. Zhou et al., 2013), and schematized modeling which systematically investigates governing processes (Best et al., 2018; Dissanayake et al., 2009; Elmilady et al., 2020; van der Wegen, 2013; van Maanen et al., 2013; Z. Zhou et al., 2016).

A common finding of these studies is that the intertidal areas accrete under SLR albeit with a time lag. The projected 21st century accelerating SLR rate increases the risk of intertidal areas drowning especially in systems with low sediment supply and systems constrained by sea defenses or geological outcrops, with no room for lateral expansion or landward migration. In natural unconstrained systems, the intertidal areas (vegetated or

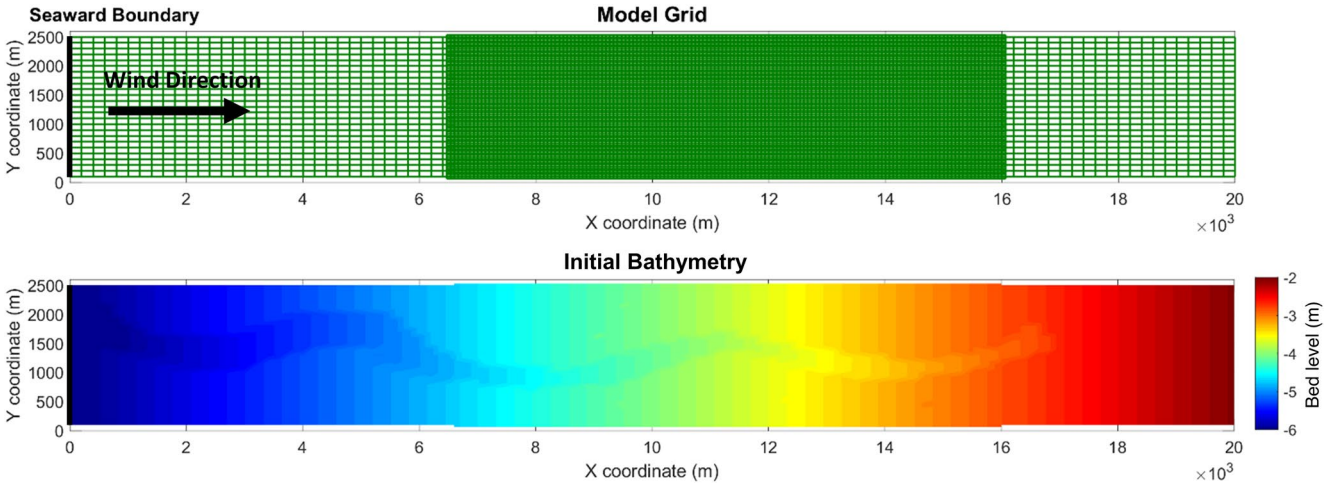

Figure 1. Model domain and the initial model bathymetry (m).

unvegetated) could be maintained if SLR causes marine transgression which depends on the available accommodation space and sediment supply (Allen, 1990; Beets & van der Spek, 2000; Townend et al., 2021).

Thus far, most modeling studies have focused on muddy environments, whereas limited attention was paid to sandy shoals. Also, sandy studies (e.g., Dissanayake et al., 2009; Lodder et al., 2019; van der Wegen, 2013) implemented coarse resolution grids and neglected wave impact as they mainly focused on the large-scale SLR impact such as basin-scale import/export trends. Elmilady et al. (2020) applied a high-resolution (≈20m grid) model of a single, fringed, sandy shoal showing the importance of detailed wave attenuation processes and tidal levee formation.

This research aims to investigate SLR impact on the long-term morphodynamic evolution of a sandy channel-shoal system in a short tidal basin (15–25 km) dominated by intertidal sandy shoals. Our main focus is on the intertidal shoal morphodynamics including the impact of wind waves and the potential presence of mud. The "intertidal shoals" investigated in this study are mainly free shoals along with some small fringing shoals in a constrained system. Although some shoals in nature may eventually develop into vegetated environments (e.g., mangrove belts, seagrasses beds, and salt marshes), our research investigates unvegetated shoals. We implement a schematized high-resolution large-scale process-based numerical modeling approach driven by main forcing conditions (tidal action, waves, and sediment supply).

2. Model Description

We schematize the system as an enclosed, non-convergent, rectangular (2.5 × 20 km) tidal basin with an open seaward boundary, see Figure 1. The model grid has an outer coarse grid (100 × 200 m) for both the seaward and landward sides and an inner fine grid (≈33 × 66 m) for the middle section. The high-resolution middle section allows for a detailed study of the shoal structure and for exploring the impact of processes related to wave attenuation and tidal levee formation that would be sub-grid in a lower resolution grid.

We apply the Delft3D (D3D) process-based numerical model in 2D mode (Deltares, 2017; Lesser et al., 2004), which solves the unsteady two-dimensional shallow water equations (momentum and continuity; Appendix A). The domain decomposition option was applied (three domains) to allow for parallel computation and to link coarse and high-resolution domains.

The initial bathymetry is a mildly sloping bathymetry from −6 to −2 m with an initial random meandering 10 cm bed level perturbation to mimic the morphology of a natural landscape that drowns due to tidal invasion. We apply an initial evenly distributed sediment mixture of two sandy sediment fractions of 100 and 250 μm representing fine and coarse fractions, with a sediment density of 2,650 kg/m^3 and a dry bed density of 1,600 kg/m^3. The implementation of multiple fractions serves to represent the variation of sediment sizes found in nature, with coarse material mainly existing in deep channels and finer fractions at shallow locations (see Figures S1 and S4 in

the Supporting Information S1 for an example showing the Wadden Sea basins' bathymetry and mean grain size). The available sediment depth was set to 20 m to allow for the evolving channels to deepen.

The seaward open model boundary was prescribed by a semidiurnal (12 hr) tidal component with an amplitude of 1.5 m mimicking a meso-tidal environment. The use of a 12 hr instead of 12 hr 25 min tidal period is for simplifying the analysis of the results and is commonly used in idealized morphodynamics modeling work (e.g., Ridderinkhof et al., 2016). The remaining boundaries are closed boundaries. This schematization represents a constrained system, with no room for lateral expansion or landward migration, which is the case in several estuaries and tidal basins around the world (e.g., Wadden Sea, Western Scheldt, and San Francisco Bay) either due to urbanization (e.g., sea defenses) or geology.

Constant suspended sediment concentrations (SSC) of 0.05 and 0.01 kg/m^3 were set at the boundary for the coarse and fine sand fractions, respectively, based on typical concentrations observed at the Wadden Sea Inlets (Postma, 1961, 1967, 1981). To avoid SSC discontinuities at the boundary during turning tides, we applied a Thatcher-Harleman relaxation time lag of 120 min (Thatcher & Harleman, 1972). The coastal boundaries option in D3D was applied to prevent the advection terms at the boundary from generating an artificial boundary layer (Deltares, 2017). To prevent instabilities by intertidal areas at the open boundary, the water depth, only at the boundary, was not allowed to drop less than 0.5 m.

The spectral wave model SWAN (Booij et al., 1999; http://swanmodel.sourceforge.net/; Appendix B) is used in stationary mode to simulate small wind-generated waves (10–20 cm) by a constant landward directed wind field of 4 m/s. The wave model covers the whole flow domain with a constant grid resolution of 100 × 200 m. No waves are prescribed at the seaward boundary, so that wave action is limited to locally generated wind waves. SWAN is coupled to D3D-FLOW through online coupling at a 30-min interval implying constant wave conditions during that interval. Each hydrodynamic time step (15 s), D3D-FLOW computes the flow including wave generated forces (F_x and F_y) as a source in the momentum equations. The Fredsoe formulations (Fredsøe, 1984) are used to compute the maximum shear stress ($\tau_{\max}$) based on the combined current (τ_c) and wave (τ_w) shear stress.

The default Van Rijn (1993) formulations are used to compute the sand transport (suspended load and bedload) for the combined effect of waves and currents. Based on the locally and time-varying velocities and water levels, the suspended sediment transport is calculated every timestep by an advection-diffusion solver which includes a sink and source term describing sediment exchange with the bed (Appendix C). Bed level changes are computed based on the divergence of the sediment transport field. Using the MORFAC approach, bed-level changes are multiplied by a morphological acceleration factor (MF) to enhance the morphological evolution. Extensive modeling studies for similar tidal systems show good results up to a MF of 400 (e.g., Braat et al., 2017; Dissanayake, 2011; Roelvink, 2006; van der Wegen & Roelvink, 2008), while wave action usually requires a lower MF.

In this research, we simulate 2 hydrodynamic years with a MF of 100 resulting in 200 years of morphological development. This MF provides stable morphodynamics with a reasonable computational effort. We perform our investigations using a configuration without (referred to as Flow simulations) and with wave action (referred to as Wave simulations). Both simulations incorporate wind forcing. The model takes about 2.5 and 4 days to simulate 1 hydrodynamic year on a 4-core (2.6 GHz) computer for the Flow and Wave simulations, respectively.

To account for bed slope effects, the streamwise and transverse bed gradient factors AlfaBs (α_{bs}), and AlfaBn (α_{bn}) were set as 1 (default) and 25, respectively, based on initial sensitivity runs within the reported range in literature. The α_{bn} is a very important parameter for the channel-shoal morphology and is often used as a calibration parameter, while model results are practically insensitive to α_{bs}. In estuarine and tidal basin models, especially when using the Van Rijn transport formulations, the α_{bn} is often set much (an order of magnitude) larger than the experimental and default values (1.5; Ikeda, 1982) to prevent the formation of unrealistically steep banks, and narrow deep channels with sharp bends (e.g., Dissanayake, 2011; van der Wegen & Roelvink, 2012).

3. Model Results

In this section, we present model results without SLR which serve as validation for our modeled morphological evolution.

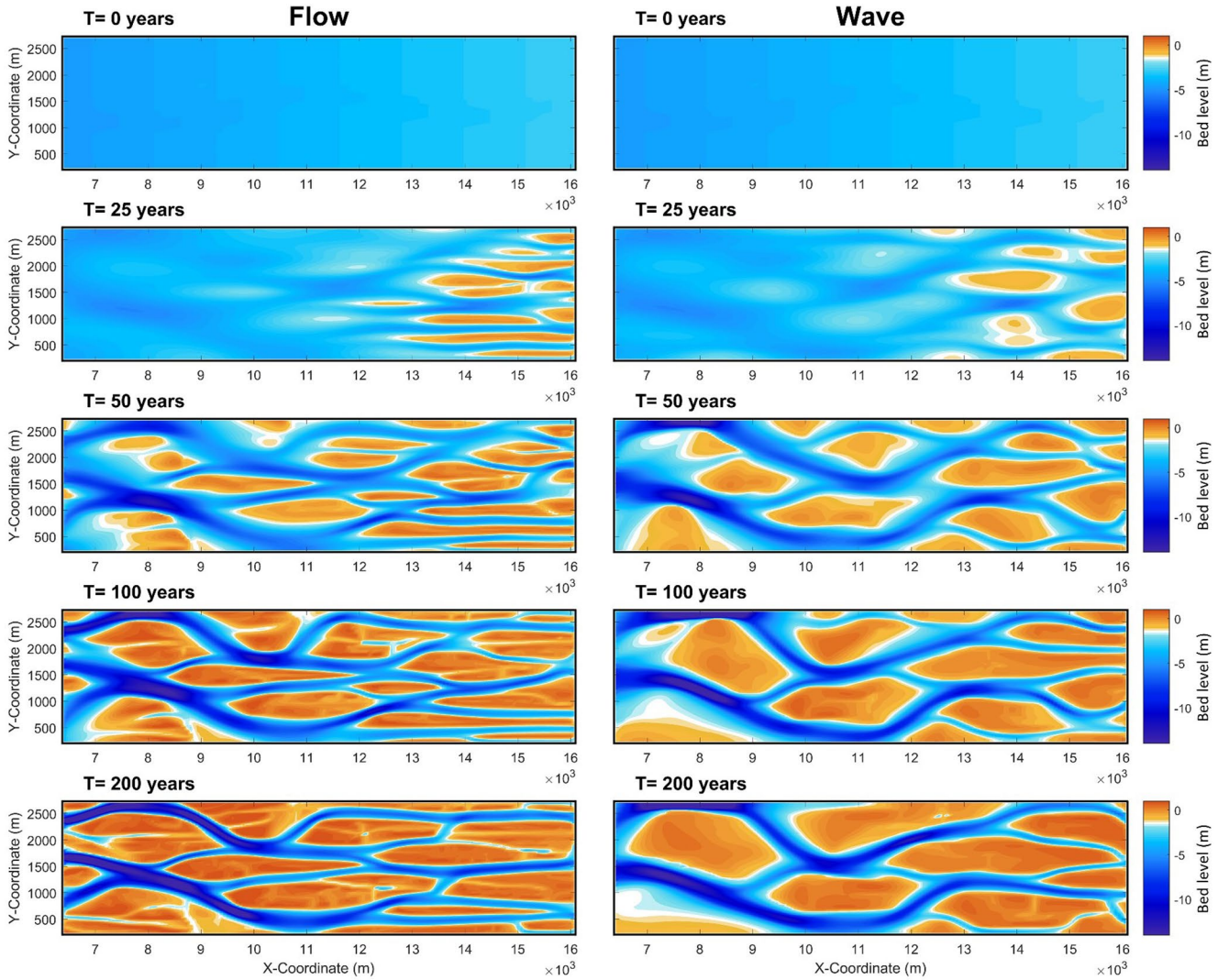

Figure 2. Modeled bathymetry (m) of the high-resolution domain over time for the Flow (left panel) and Wave (right panel) simulations. The white color band is the average low water level (LW ≈ −1.6 m) which indicates the approximate border between the intertidal (shoal) and subtidal (channels) areas.

3.1. Morphology

We simulate the morphological evolution of the initial bathymetry for 200 years toward a stable channel-shoal system (Figure 2). Over time, channel-shoal patterns emerge eventually creating intertidal areas. The morphological development is rapid in the beginning but gradually decreases over time leading to a state of low morphological activity. Movie S1 shows an animation of the channel-shoal system evolution over time.

For both Flow and Wave simulations, shoals develop at roughly the same locations. The end morphologies (T = 200 years) show that the Wave simulation leads to more coherent, lower elevation shoals with fewer intersecting channels and a smoother surface than in the Flow simulations. The Wave simulation also shows wider and shallower channels.

Previous studies (e.g., Allen & Duffy, 1998; Carniello et al., 2005; Elmilady et al., 2020; Fagherazzi et al., 2007) provide an explanation for this. Flood tides supply sediments to the shoals that deposit near the channel-shoal edge as tidal levees. These sediments are re-suspended by wave-induced shear stresses at lower water levels. Subsequent flood flows then transport the re-suspended sediments further on to the shoal.

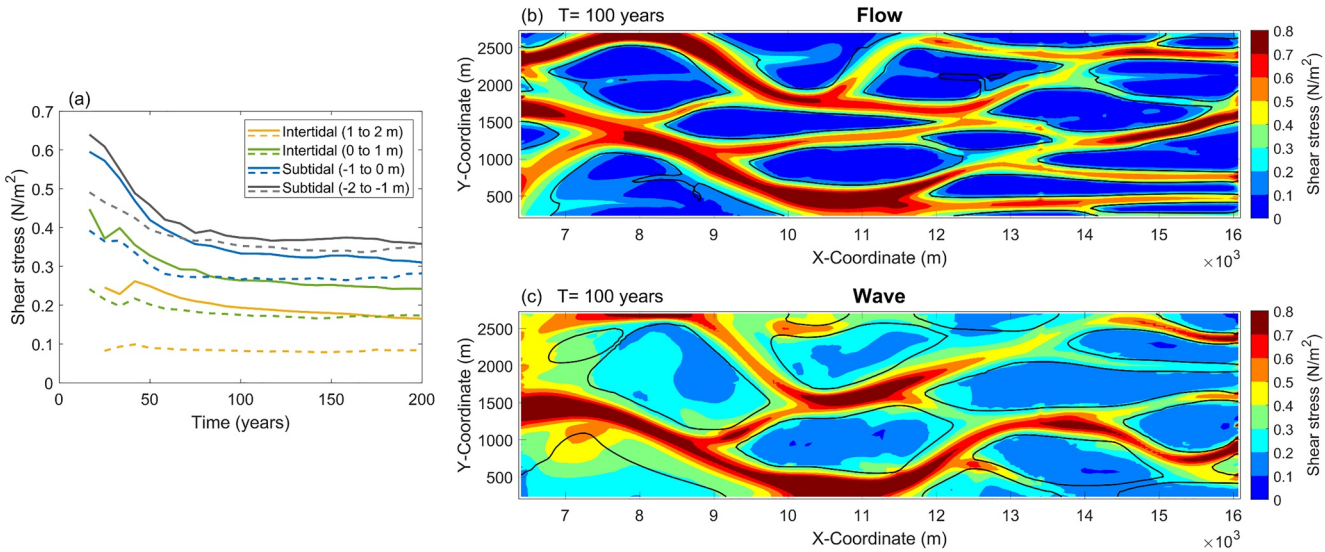

Figure 3. (a) Temporal development of $\bar{\tau}_{max}$ (N/m^2) spatially averaged over the whole model domain and over 1 m vertical elevation bins. The bin range is with respect to LW and is divided into subtidal bins (−2 to −1 m; gray, and −1 to 0 m; blue), and intertidal bins (0 to 1 m; green, and 1 to 2 m; yellow). Solid and dotted lines correspond to Wave, and Flow simulations, respectively. Panels (b, and c) $\bar{\tau}_{max}$ map of the high-resolution domain at T = 100 years for the Wave, and Flow simulations, respectively. The black contour lines indicate the border (LW) between intertidal and subtidal areas.

3.2. Shear Stresses

For both simulations, the tidally averaged maximum shear stresses ($\bar{\tau}_{max}$) is highest at the beginning as the initial shallow bathymetry causes high flow resistance (Figure 3a). As shoals start emerging and gain elevation, the flow gets redirected into the deepening channel. The $\bar{\tau}_{max}$ over the shallow sections gradually decreases with time toward a relatively stable state.

Waves increase the maximum shear stresses over the shoals. The wave impact (the difference between the solid and dashed identical color lines in Figure 3a) on the $\bar{\tau}_{max}$ is highest at the shallow intertidal areas and gradually decreases with depth. On the other hand, the highest $\bar{\tau}_{max}$ occurs at the deep subtidal channels and decreases toward the shallow intertidal areas (Figures 3b and 3c). Movie S2 shows the development of Figure 3 over time.

3.3. Sediment Transport

The initial bed level perturbation creates variations in the currents and sediment transport. This triggers a morphological feedback in which tide-residual sediment transport convergence accretes the shoals and sediment transport divergence deepens the channels. The emergence of intertidal areas decreases the tidal prism and the tidal asymmetry which favors flood dominance and landward-directed tide-residual sediment transport. Also, the channel deepening decreases the depth-averaged SSC levels. Over time, the residual transport gradually diminishes resulting in a stable channel-shoal system. As an example, Figure 4 shows the residual sediment transport magnitude and direction for the Wave simulation at a state of low morphological activity after 150 years. The presented sediment transport throughout this paper is the total transport (bed and suspended). The bed transport is highest at the initial stages of the channel-shoal formation. Over time, the bed transport decreases and becomes an order of magnitude smaller than the suspended transport. Movie S3 shows the 200-year temporal development of Figure 4 along with the corresponding development for the Flow simulation.

3.4. Wave Impact

Tide-residual sediment transports generate channel-shoal patterns, while wave action only becomes important when shoals emerge. To explore the long-term impact of waves on the shoal morphology, we subjected the 150-year modeled Wave morphology to a 50-year variation in the wave forcing (Figure 5). Three wave conditions were investigated: (a) no waves; (b) 10–20 cm waves (continuation of Wave Base-case normal forcing); (c) 15–25 cm waves (increased wave action).

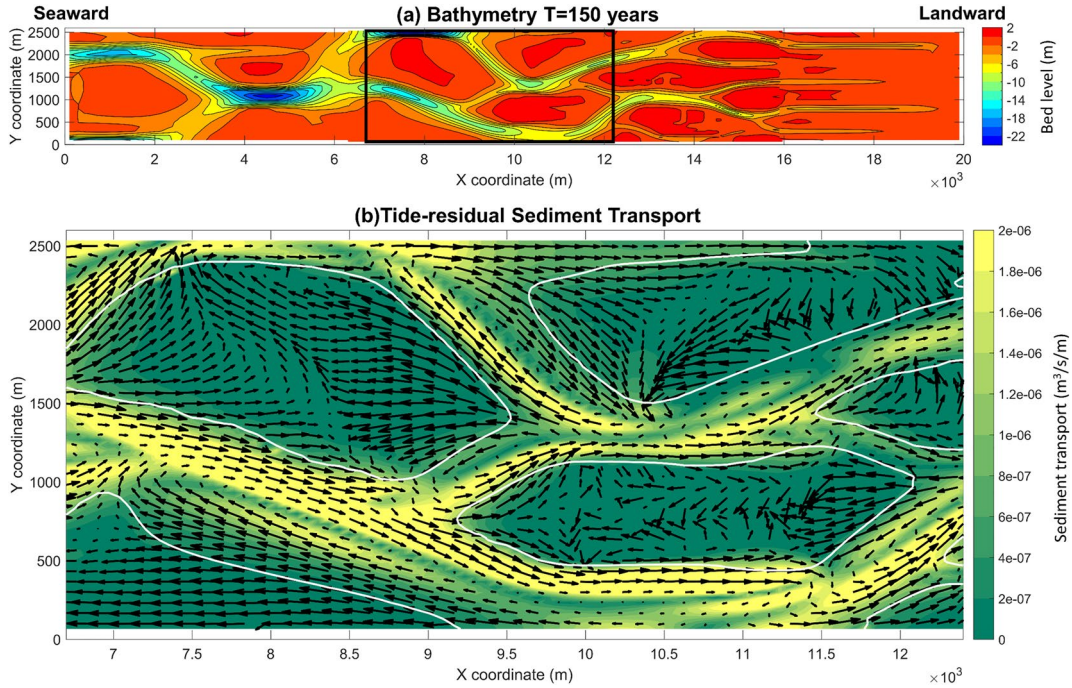

Figure 4. (a) The modeled bathymetry (m) at T = 150 years for the whole model domain. The black box indicates the location of the bottom plot. (b) The tide-residual sediment transport magnitude ($m^3/s/m$) and direction. Arrows are RMS normalized and plotted on a grid with half the model grid resolution to make them more visible. The white contour lines indicate the border (LW) between the intertidal and subtidal areas.

The variation of wave conditions only had an impact on the shoal area and elevation. Excluding waves (Figures 5b, 5e and 5h) resulted in the largest area and highest elevation shoals with high elevation ridges at the shoal edges and drainage channels on top of the shoal. The highest accretion occurs at the shoal edge and decreases going landward. This can be explained as the profile accretes over time, the cross-shore velocities over the shoal start gradually dropping until they are not strong enough to resuspend the sediment supplied by the channels and distribute it across the shoal. In the absence of wave-induced resuspension, the sediment accumulates at the shoal edge causing the formation of high elevation ridges (tidal levees) and a seaward extension of the shoal (widening). Wang et al. (2018) show that tidal levee features are indeed found on sandy shoals in Dutch estuaries, although they may be short-lived due to strong variations in wave action. On the other hand, for the increased wave action case (Figures 5d, 5g and 5j), the higher wave shear stresses resulted in the smallest area and lowest elevation shoals with the smoothest surface and limited drainage channels. For all forcing conditions, the morphodynamic activity decreases over time which suggests that it is approaching an equilibrium state.

4. Sea-Level Rise

SLR is imposed as a rise of the MSL over 100 years, starting from the modeled morphology at T = 100 years to T = 200 years (Figure 6). At this stage (T = 100 years), the system has reached a relatively stable state with limited morphological activity which allows for investigating and isolating the SLR impact. We explore four SLR scenarios; the rise is imposed either as a non-linear rise (0.96, 1.67, and 2.63 m/century) based on a sinusoidal function rising from the minimum to the intercept or as a linear rise with a constant rate (0.96 cm/yr). The SLR magnitude is based on high-end global SLR probabilistic projections by Le Bars et al. (2017) which includes the potential rapid loss of the Antarctic ice sheet mass. The 0.96 m is maybe the most likely scenario and corresponds to the 50th percentile of the representative concentration pathway scenario RCP4.5, while the 1.67 and 2.63 m correspond to the 50th and 95th percentile of the RCP8.5 scenario, respectively.

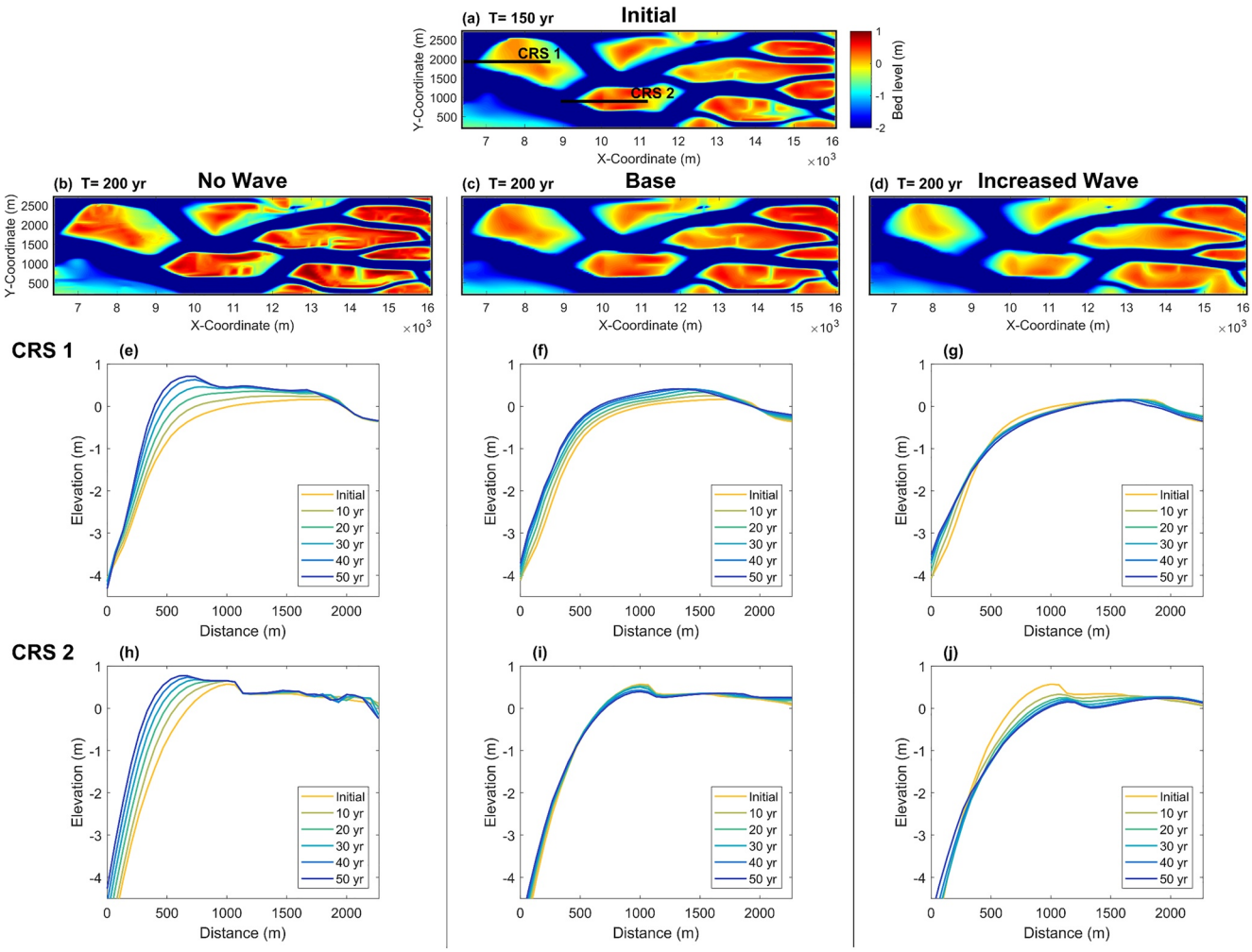

Figure 5. (a) The initial bathymetry (m) (Wave simulation; T = 150 years) along with the location of the two cross-sections (CRS 1, and CRS 2). The modeled bathymetry after 50 years of (b) no waves, (c) Base-case waves, and (d) increased waves. The cross-sectional profile development over time for CRS 1 (e, f, and g), and CRS2 (h, i, and j) for the three wave scenarios. The profiles were chosen parallel to the wind field direction and on the upwind side of the shoals which is subjected to the highest wave attack.

4.1. Morphology

SLR notably impacts the shoal morphology. Figure 7 shows the 0.96 m non-linear SLR impact on the shoal morphology for the Base Wave (BW; a, b, c, d, and e), and the Base Flow (BF; f) simulations. The initial bathymetry of the BF run (not shown) is the 100-year bathymetry of the no SLR run with Flow. Comparing Figures 7a with 7b shows that limited morphological change occurs during the 100 years with no SLR, while shoals accrete significantly in case of SLR (Figure 7c). Figure 7d shows that shoals remain at approximately the same locations while experiencing more accretion (red color) under SLR. Spatial variations exist in the accretion magnitude. Shoal accretion is highest near the seaward boundary (basin sediment source). On the shoal scale, accretion is highest at the shoal edges near the channels (shoal sediment source). This causes the formation of high elevation ridges (tidal levees) at the shoal edges.

In most locations, the accretion magnitude is less than the SLR magnitude. Correcting the shoal elevation with the SLR magnitude (Figure 7e) and comparing it with the No SLR elevation (Figure 7b) shows that the intertidal shoal areas experienced a notable decrease in their relative elevation and a slight decline in their areal extent.

In general, we see the same response from the Flow simulation under SLR. A major difference is that much shoal accretion occurs near the channel-shoal interface leading to more pronounced levee formation at shoal edges (Figure 7f and Figure S5 in the Supporting Information S1), while waves lead to smoother intertidal flats.

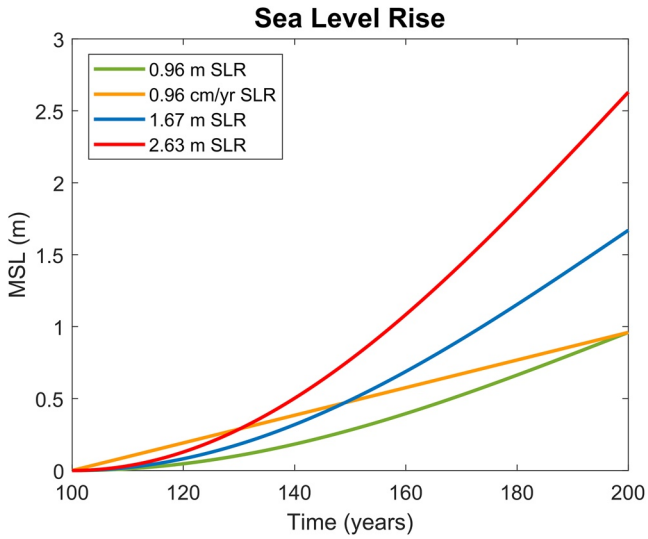

Figure 6. The mean sea level (MSL; m) for the implemented sea-level rise scenarios.

4.2. Hydrodynamics and Sediment Transport

Figure 8 shows the SLR impact on the hydrodynamics and sediment transport, the presented SLR results are for the 0.96 m non-linear scenario as it is the most likely scenario. Other SLR scenarios have the same impact, albeit with different magnitudes (see Figure S6 in the Supporting Information S1). We present the maximum flood and ebb velocities in the plots because their difference shows a good correlation with the tide-residual transport magnitude and direction since the majority of sediment transport occurs during or in the vicinity of peak flow.

Both flood and ebb velocities increase due to an increase in the tidal prism under SLR (Figures 8c–8f). The increase in the tidal prism is mainly due to the inundation of intertidal areas along with a slight increase in the tidal range. For example, for the 0.96 m SLR, at the seaward border of the presented domain (e.g., Figure 8c), the tidal prism increased by 18% and the tidal amplitude increased by approximately 1.5%, while the tidally averaged cross-sectional volume increased only by 9%. In addition to the increase of flow velocities, SLR enhances the tidal asymmetry favoring flood dominance. The increase in flood velocities is larger than that for the ebb velocities (Figures 8g–8h). Also, the flood duration is shortened while the ebb duration is elongated (Figure S7 in the Supporting Information S1). This increased asymmetry is caused by the inundation of the intertidal areas.

Changes in the system's hydrodynamics under SLR notably impact the tide-residual sediment transports (Figure 8i and 8j). Without SLR, the residual sediment transport gradually diminishes over time leading to a state of low morphological activity (Figure 8i). The SLR-induced increase in flow velocities elevates the SSC levels in the system (Figure S8 in the Supporting Information S1). This combined with the increased flood dominance with SLR results in a notable landward tide-residual sediment transport and sediment import to the system (Figure 8j). The majority of the sediment import to the system is composed of the fine sand fraction.

4.3. Sensitivity Analysis

We performed a sensitivity analysis to explore the SLR impact with different forcing conditions such as SLR scenarios (set 1, and 2), wind-wave activity (set 3), tidal forcing (set 4), sand supply (set 5), and the inclusion of mud fractions (set 6), Figure 9. The sensitivity analysis was carried out based on the two Base-case simulations discussed in Section 4.1; Base Flow (BF; set 1), and Base Wave (BW; set 2 to 6). The shoal and channel volumes are calculated based on a fixed datum (LW) of the No SLR case. This allows for visualizing the impact of SLR on the morphology while excluding the state changes between shoals and channels which is caused by the SLR-induced increase in the water level. The shoal volume (m^3) is defined as the sediment volume above LW, while the channel volume (m^3) is defined as the water volume below LW. For example, an increase in shoal volume indicates depositional shoals, while a decrease in channel volume indicates channel infilling.

4.3.1. Sea-Level Rise Scenarios

The SLR-induced sediment import to the system results in notable deposition on the shoals and in the channels. The shoal volume increases while the channel volume decreases (Figure 9; set 1, and 2). The increase/decrease magnitude depends on the SLR magnitude and rate. Higher SLR results in more sediment import. Also, a linear SLR causes more deposition compared to a non-linear rise. For the linear SLR, during the entire simulation period, the SLR magnitude is higher than that for the non-linear SLR which only reaches the same magnitude at the end (see Figure 6). This allows the system with the linear rise more time to adapt to the imposed SLR thus resulting in higher accretion. Elmilady et al. (2020) note this behavior and highlight a faster adaption to the linear rise.

Figure 10 shows the temporal development of the shoal and channel volume and area for the Wave simulations under the different SLR scenarios. The dashed lines are based on a fixed reference (LW), while the solid lines are based on a moving datum with the SLR (LW + SLR). In this section, parameters (e.g., shoal volume) based on the moving datum are referred to as "relative" parameters as being relative to the SLR.

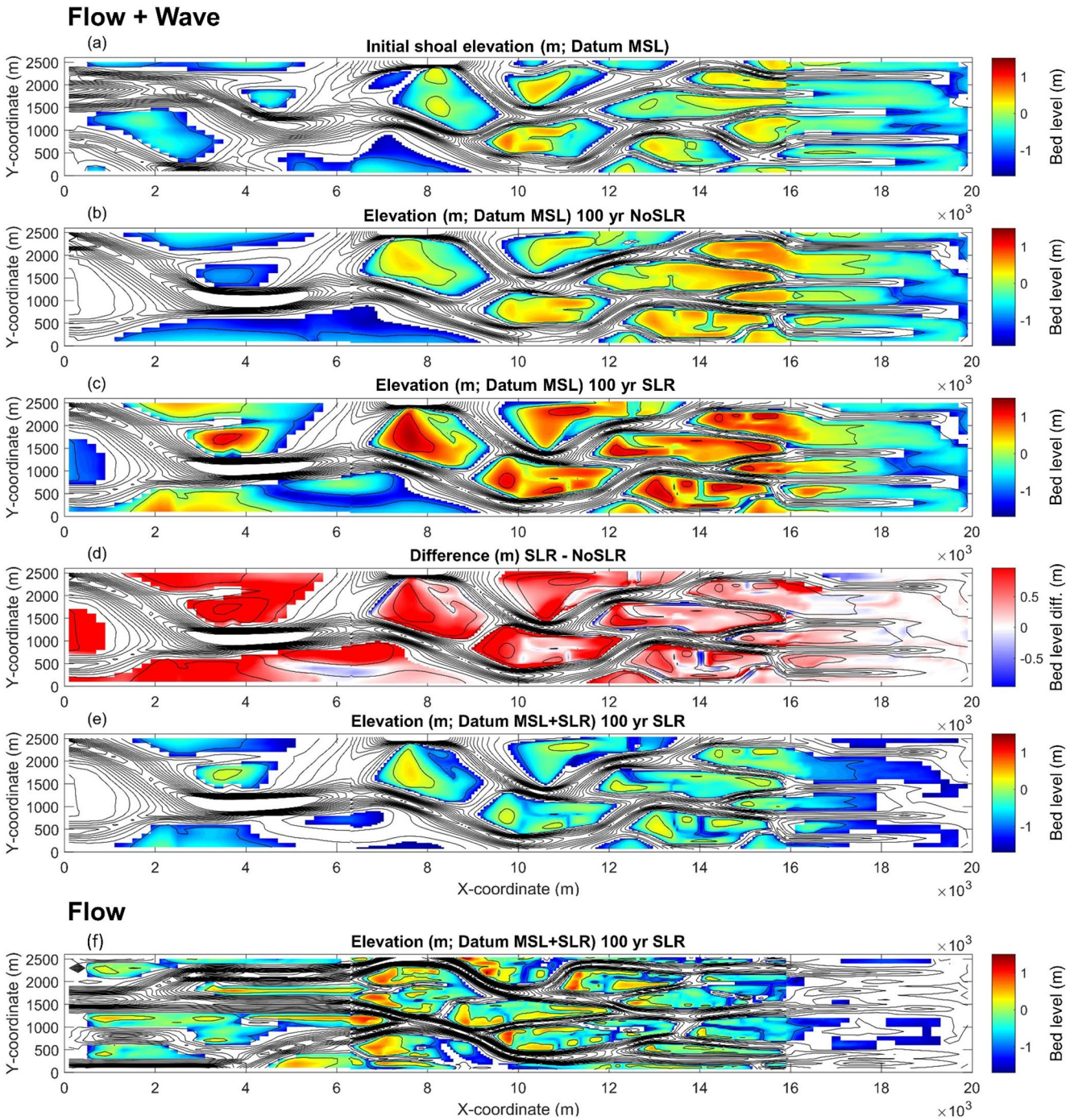

Figure 7. Sea-level rise (SLR) impact on the shoal morphology for the simulation including wind-wave impact (a, b, c, d, and e; Base Wave; BW). (a) The initial shoal elevation (m; with respect to mean sea level (MSL)), (b) the shoal elevation (m; w.r.t MSL) after 100 years with no SLR, (c) the shoal elevation (m; w.r.t MSL) after 100 years with a non-linear 0.96 m/century SLR, (d) the difference between the shoal elevation for the SLR and No SLR scenarios (color bar from −0.96 to 0.96 m), and (e) the shoal elevation (m; w.r.t MSL + SLR) corrected with the SLR magnitude. (f) The shoal elevation (m; w.r.t MSL + SLR) corrected with the SLR magnitude (0.96 m) but for the simulation excluding wind-wave impact (Base Flow; BF). The black lines are the elevation contours with 1 m intervals.

SLR induces shoal deposition with higher magnitudes with the increasing SLR leading (Figure 10a; dashed lines). However, accounting for the SLR-induced rise in the water levels, the relative shoal volume (Figure 10a; solid lines) decreases for all scenarios. The morphodynamic adaptation lags behind SLR as accretion rates do not match the SLR rate. For all the non-linear SLR scenarios, this lag continues to increase with the accelerating

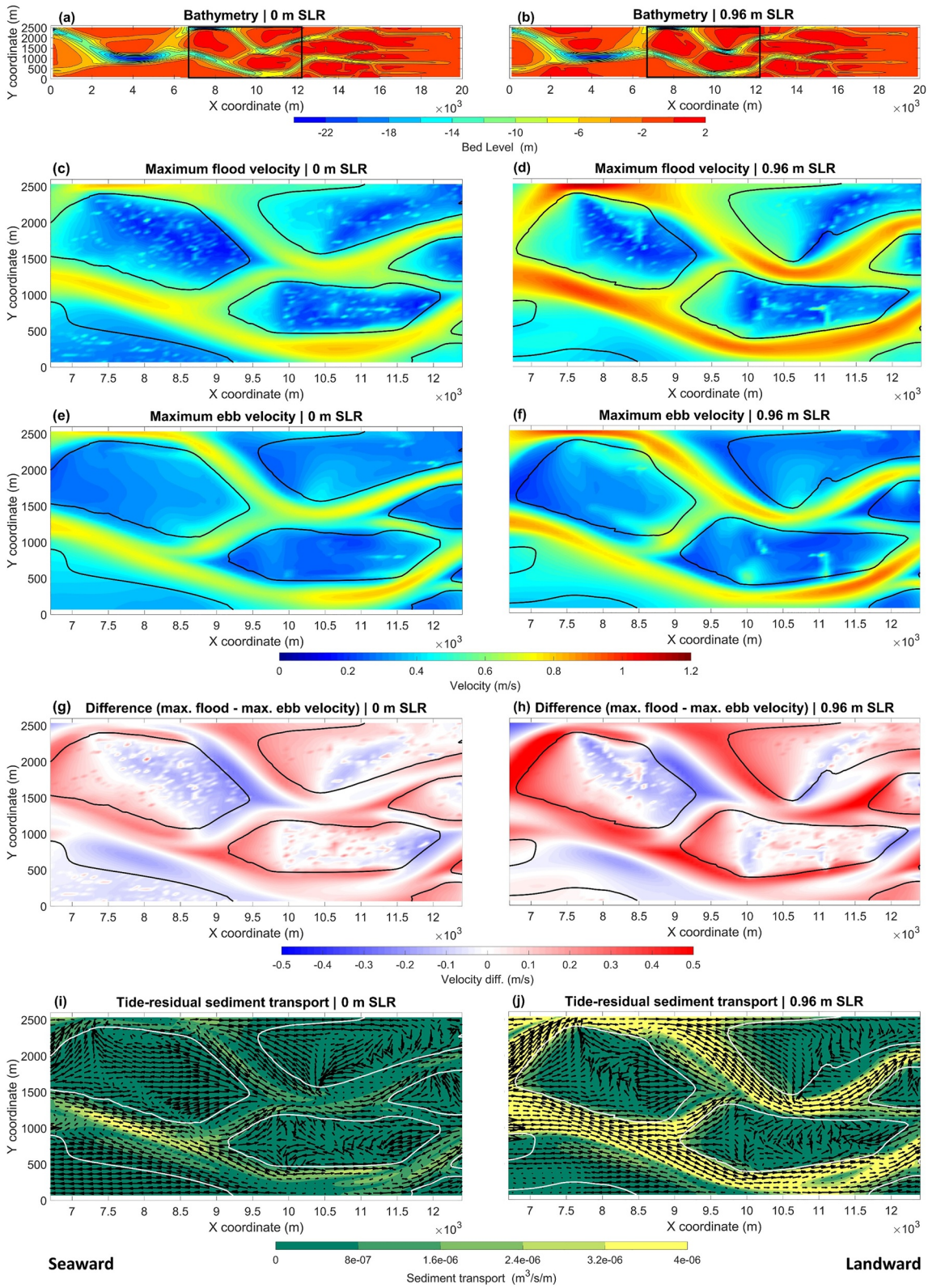

Figure 8. The modeled bathymetry (m) for the Wave Base-case simulation after 100 years with (a) no sea-level rise (SLR), and (b) 0.96 m SLR. The black box indicates the location of the below plots. (c, and d) Maximum flood velocities, (e, and f) Maximum ebb velocities, (g, and h) difference between maximum flood and ebb velocities, and (i, and j) the tide-residual sediment transport magnitude ($m^3/s/m$) and direction. Arrows are RMS normalized and plotted on a grid with half the model grid resolution to make them more visible. The black/white contour lines indicate the border (LW) between the intertidal and subtidal areas.

Figure 9. Summary of the sensitivity analysis for different forcing conditions showing (a) the shoal volume (m^3; w.r.t LW), and (b) the channel volume (m^3; w.r.t LW) for the whole model domain for the initial state (blue), after 100 years without sea-level rise (SLR) (Orange), and after 100 years with SLR (Green). The legend presents the abbreviations used for the different simulations and the description of the varying forcing condition. BF and BW refer to the Base Flow and Base Wave simulations, respectively.

SLR which leads to continuous shoal drowning. Remarkably, the linear constant SLR rate (0.96 cm/yr), experienced the least shoal volume decline. There is an initial loss of the relative shoal volume in the first ≈50 years which gradually flattens and follows the No SLR signal when the SLR-induced accretion rates start approaching the constant SLR rate. This behavior has been noted in previous modeling studies with ASMITA (Van Goor et al., 2003; Wang & Roelfzema, 2001) and D3D (Elmilady et al., 2020). It represents the system's adjustment to the "initial" perturbation due to the introduction of SLR and a need to establish an "overdepth" to generate a new dynamic equilibrium that follows the SLR at the same rate.

SLR also favors channel deposition with higher magnitudes under increasing SLR (Figure 10b; dashed lines). However, the SLR-induced rise in the water levels causes an increase in the relative channel volume (Figure 10b; solid lines). Similar to the shoal volume, the non-linear SLR resulted in the least relative channel volume increase.

SLR causes a drop in the relative shoal area and an equivalent increase in the relative channel area (Figure 10c and 10d; solid lines). For instance, by the end of the simulation, the relative shoal area became 12.5% (0.96 m linear SLR) to 51.5% (2.63 m non-linear SLR) smaller than that for the No SLR scenario.

For all SLR scenarios, the percentage of the relative shoal volume decrease (Figure 10a; solid lines) is higher than that for the relative shoal area decrease (Figure 10c; solid lines) thus resulting in lower elevation surviving shoals. For example, with the 2.63 m SLR scenario, SLR caused a decrease in the relative shoal volume and area of 77% and 51.5%, respectively, leading to a drop in the average relative shoal elevation (w.r.t LW + SLR) from 1.22 m with No SLR to 0.57 m with SLR. On the other hand, SLR caused an increase in the relative channel volume and area of 31% and 67%, respectively, leading to a drop in the average relative channel depth (w.r.t LW + SLR) from

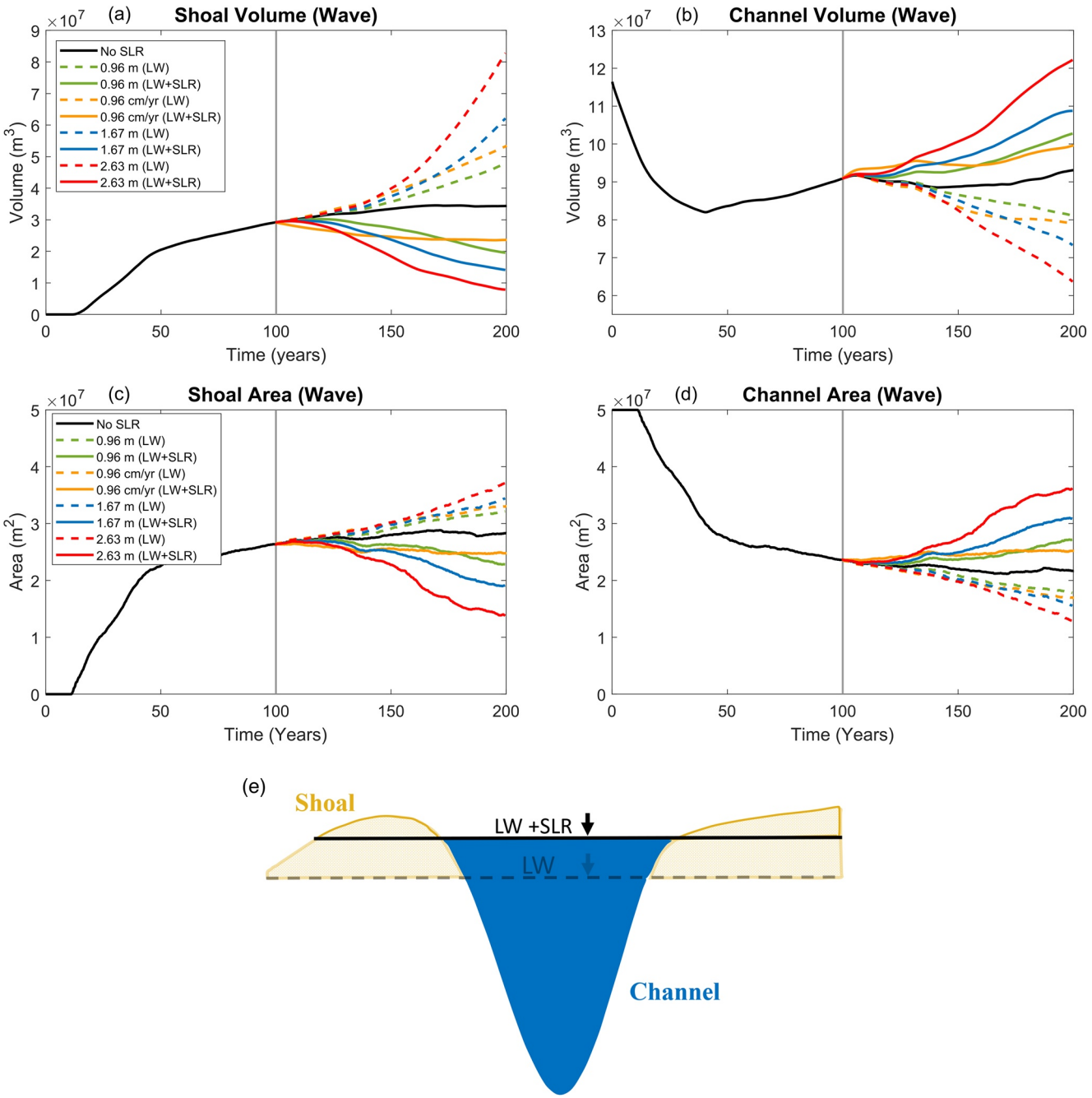

Figure 10. The temporal development of the shoal (a) and channel (b) volume (m^3) and the shoal (c) and channel (d) area (m^2) for the whole model domain and for the Wave simulations. The solid black line is the No sea-level rise (SLR) scenario, while the color lines are for the different SLR scenarios. (e) Schematic showing the shoal and channel definition along with the datums used for the dashed lines (fixed datum; LW), and the solid lines (moving datum; LW + SLR).

4.3 m with No SLR to 3.4 m with SLR. The main reason behind this relative depth decrease is that the SLR-induced increase in water level changes a large portion of the intertidal areas to shallow channels. However, the whole domain is becoming deeper with SLR, especially the deepest subtidal sections.

Flow simulations (Figure S9 in the Supporting Information S1) show a trend of morphological evolution under SLR that is similar to the Wave Simulations (Figure 10). A difference is that, for all SLR scenarios, Flow simulations experience larger channel deposition. For the Flow linear SLR, the relative channel volume even turns from increasing to decreasing. The reason behind this is that shoal accretion in the flow simulations mainly occurs at

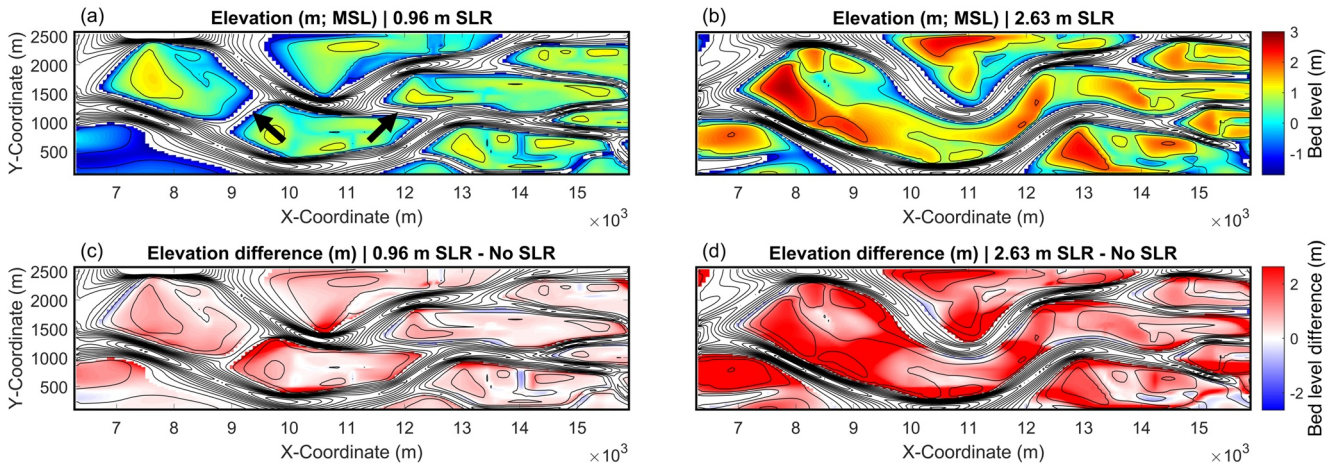

Figure 11. (a, and b) The shoal elevation (m; w.r.t mean sea level) for the 0.96, and 2.63 m non-linear sea-level rise (SLR), respectively. The black arrows in (a) point to the location of the secondary channels. (c, and d) The shoal elevation difference (m) between the SLR and No SLR scenario. The plots are for simulations including wave action.

the channel-shoal interface (see Section 4.1). The SLR turns a portion of this area into shallow channels thus this deposition is considered as channel accretion. Also, since most of the SLR-induced accretion is composed of the fine fraction (Section 4.2), this makes channels in Flow simulations more likely to experience sediment fining which impacts the equilibrium channel volume (decreases).

SLR can impact the large-scale channel-shoal patterns. As shown before in Figure 7, this impact is minimal for the 0.96 m non-linear SLR. Shoals remained in approximately the same location while experiencing accretion and slightly losing intertidal area from their edges. The SLR impact on the spatial patterns becomes more pronounced with the higher SLR scenarios (e.g., Figure 11 including wave action). The secondary shallow channels (black arrows in Figure 11a) connecting the two main deep channels experience notable deposition which results in shoals merging. Figures 11 a, and b show the morphology not corrected with the SLR magnitude. A large section of the merged shoal is not intertidal since only specific locations can keep pace with the SLR and do not drown.

The hypsometry curves and the shoal slopes for the Flow and Wave simulations are presented in the Supporting Information (Figures S10, and S11, Text S2 in the Supporting Information S1).

4.3.2. Wave Action

In the Base-case Wave simulation (BW) we implement a constant (4 m/s) wind field, while in nature the wind field varies continuously. Also, in the Wadden Sea region, the average wind speed ranges from 6 to 7 m/s (Brinkman et al., 2001; KNMI, 2014). Modeling a high wind speed (>6 m/s) requires decreasing the morphological factor (MF), especially during the initial period (≈100 years) with high morphological activity. The Base-case value of 4 m/s allows for performing a sensitivity analysis without extensive simulation times and with equal MFs. In this section, starting from the BW initial (T = 100 years) morphology, we investigate different wind conditions including lower, higher, and time-varying wind speeds. The spatially (over the model domain) and temporally averaged wave-orbital velocity squared (u^2_{orb}) was used as a metric to compare the wave action between the different simulations. For the No W simulation, there is no wave action. The constant base wind speed of 4 m/s (BW) creates approximately equivalent wave action to a varying wind speed from 2 to 5.35 m/s (W1). Text S1 and Figure S12 in the Supporting Information S1 provide more information regarding the variable wind speed implementation and the wave orbital velocities.

Model results suggest that the largest wave action leads to the highest SLR shoal adaptation capacity, albeit that the resulting morphology is different. Figure 9; set 3 shows the shoal and channel volume for the different wind-wave conditions. Variations in wind-wave activity mainly impact the shoal volume, while the impact on the channel volume is relatively low. Compared to the BW simulation, excluding waves (No W) resulted in larger shoal deposition without SLR which is further enhanced by SLR. Time-varying conditions (W1) with an approximately equivalent wave action resulted in similar shoal deposition magnitudes to that of the BW both with and without SLR. The increased wave action (W2) resulted in slight shoal erosion with No SLR, however, similar to the other

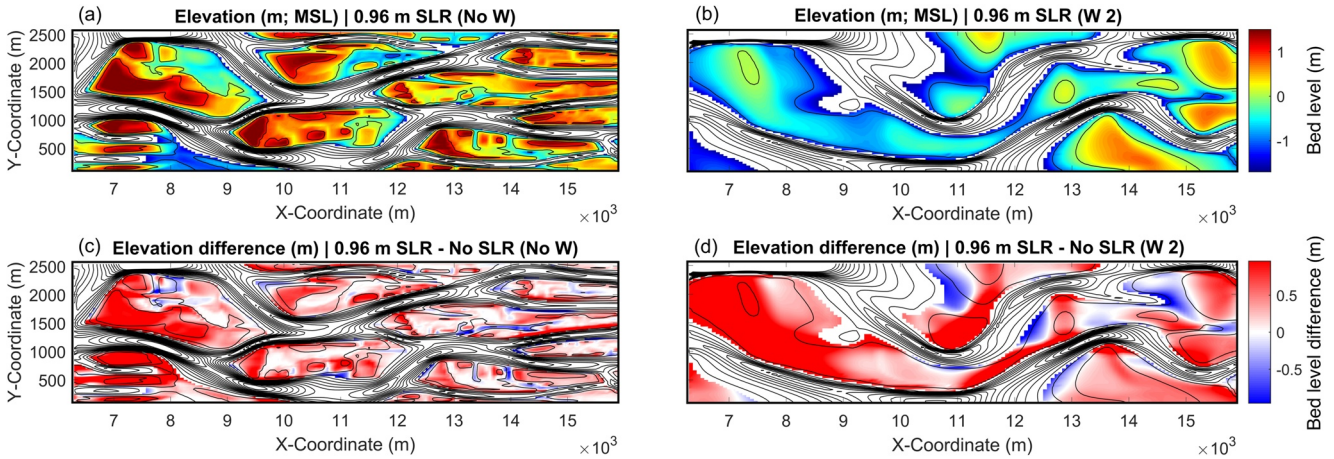

Figure 12. (a, and b) The shoal elevation (m; w.r.t mean sea level) for the No W and W2 wind-wave conditions, respectively. (c, and d) The shoal elevation difference (m) between the sea-level rise (SLR) and No SLR scenario for each wind-wave condition.

conditions, SLR induces shoal deposition. The SLR-induced shoal deposition magnitudes for the No W, BW, and W2 are 1.23, 1.35, and 1.18 × 10^7 m^3 which represent a 29%, 39%, and 50% increase to their No SLR shoal volume of 4.25, 3.43, and 2.38 × 10^7 m^3, respectively.

Similar to the noted behavior when starting from different initial bathymetries (Section 4.1), wave action exclusion (Figures 12a and 12c) resulted in spatial variations in the SLR-induced shoal accretion with the highest accretion occurring at the shoal edges. On the other hand, the highest wave action (Figures 12b and 12d) resulted in the most uniform accretion and the smoothest shoal morphology under SLR. This is caused by the added wave shear stresses which enhance sediment resuspension and distribution over the shoal (see Section 3.4). In addition to the shoal-scale impact, waves also enhance the sediment distribution along the basin's longitudinal axis. This leads to larger accretion and faster adaptation of landward shoals to SLR.

Despite the differences between the two opposite end situations (without waves and with high wave action), the system reacts to the SLR in the same manner. Also, a constant wind speed showed similar results to an approximately equivalent wave action generated by a time-varying signal.

4.3.3. Tidal Forcing

We investigated the impact of the tidal range (dH) on the morphological response to SLR by comparing the Base-case wave simulation (BW; dH = 3.0 m) to other simulations with lower (dH = 2.5 m) and higher (dH = 3.5 m) tidal range (Figure 9; set 4). Unlike the waves, the change in the tidal range notably impacts the channel volume. Without SLR, a drop in the tidal range (dH = 2.5 m) resulted in a notable channel volume decrease due to deposition, while an increase in the tidal range resulted in a notable channel volume increase due to erosion. This response represents the system's adaptation to the newly imposed forcing conditions that deviate from the original forcing. The increase in tidal range causes higher channel flow velocities which leads to channel deepening. This is the only simulation in which the system shifted from a slightly importing system to being an exporting system. The opposite happens with the drop in tidal range leading to an increase in the sediment import and to shallower channels.

Despite the different morphodynamic evolution of the channel, in all simulations, the system responds to SLR in the same manner. SLR induces sediment import in the system resulting in channel deposition thus leading to shallower channels compared to the No SLR case. For the dH 2.5 case, the SLR-induced channel deposition (1.78 × 10^7 m^3) is notably higher than the dH 3.5 case (1.07 × 10^7 m^3). The reason is that for the dH 2.5 case there are two forcing changes that are enhancing sediment import to the system, the SLR and the drop in tidal range. While for the dH 3.5, the SLR-induced import is opposing the export trend caused by the increase in dH. With regard to the shoal volume, SLR causes an increase in shoal volume due to deposition, again this increase is more pronounced in the case of dH 2.5 for the same above indicated reason.

In addition to the tidal range, we also investigated the impact of a lunar spring-neap tidal cycle (LUN) and a schematized mixed semi-diurnal tidal cycle (MS) by implementing the tidal constituents M_2 with S_2, and M_2 with C_1 (artificial constituent combining K_1 and O_1; Lesser, 2009), respectively. The amplitudes for the M_2, S_2, and C_1 are 1.5, 0.4, and 0.2 m, respectively. The ratios between the tidal amplitudes are based on Wadden Sea conditions (Herrling & Winter 2015). We assume no phase differences between the constituents.

Results show a similar SLR adaptation as the base case (BW) simulation, albeit with different magnitudes. For the LUN case, without SLR, the increased tidal range/flow velocities during the spring tides resulted in deeper channels (lower channel volume). However, the SLR adaptation remained the same with channels and shoals experiencing accretion. For the MS case, the small amplitude of the diurnal signal (0.2 m) resulted in limited differences compared to the BW simulation with the semi-diurnal signal.

It is important to note that the values presented in Figure 9 (set 4) are not corrected for the change in LW (border between shoals and channels) due to the change in the tidal range between the simulations. The only difference is the volume magnitude based on what is considered shoals and channels. However, the SLR impact on the morphological development and the noted differences between the simulations does not change when implementing the corrections.

4.3.4. Sand Supply

We investigated the impact of the sandy sediment supply on the morphological adaptation to SLR (Figure 9; set 5). We implemented lower (LS) and higher (HS) sand supply scenarios compared to the BW simulation by increasing and decreasing the open boundary SSC of the fine sand fraction by 50%, respectively. Without SLR, the decrease and increase in sediment supply mainly impacted the channel volume causing larger, and smaller volumes compared to the BW, respectively. For all sand supply scenarios, shoals and channels accrete in response to the SLR. However, the SLR-induced accretion is notably higher for the HS case than that for the LS. The shoal and channel accretion for the HS (1.68×10^7 and 1.67×10^7 m^3) is more than 2 and 3.5 times than that for the LS (0.77×10^7 and 0.45×10^7 m^3), respectively.

4.3.5. Mixture Sand and Mud Fractions

In most sand-dominated estuarine environments and tidal basins, fine mud fractions are present as well in sheltered low-energy locations (e.g., Colombia River Estuary; Sherwood & Creager, 1990, Western Scheldt Estuary; Kuijper et al., 2004, and Wadden Sea; Postma, 1957). We thus explored the impact of mud presence on the morphological response to SLR. Starting from an initial sandy bed (BW), we impose a mud fraction as a small constant concentration (20 mg/l) at the model seaward boundary. For these mixture runs, we simulate two situations of 100 years without and with 0.96 m/century nonlinear SLR. The mud transport is modeled using the Partheniades Krone formulations (Partheniades, 1965; Appendix C). This implementation accounts for the mud impact on the sand erodibility but not vice versa. The applied mud fractions have a critical erosion shear stress ($\tau_{c,e}$) of 0.25 N/m^2, an erosion parameter (M) of 2.0×10^{-4}, and a settling velocity (w_s) of 0.5 mm/s for simulation Mix1 and 1 mm/s for simulation Mix2.

Figure (9; set 6) shows that, without SLR, the inclusion of mud results in more deposition in the model domain reflected by a larger shoal volume and less channel volume. This increase in sediment import to the system is due to the higher and finer SSC (sediment supply) imposed at the seaward boundary in the case of the mixture.

Sediment supplied at the seaward boundary needs time to reach landward locations (Figures 13b and 13d). With the sand fractions, the landward-directed sediment transport is slower than with the finer mud fractions that can remain in suspension for a longer duration. This results in a larger deposition gradient along the basin axis for the sandy case. Mud inclusion resulted in a notably larger deposition at the landward section (10–20 km) along with lower deposition at the more energetic seaward section. For the mixture cases, shoals experienced more SLR-induced deposition than the sandy case due to mud deposition. On the other hand, the channel deposition is lower as mud fractions are less likely to settle in the deep channels.

Figure 14 shows the mud percentage in the top sediment layer (0.25 m) for Mix1 and Mix2 with and without SLR. Mud fractions mainly settle on the shoals while the channels with larger flow velocities remain relatively mud-free. Without SLR, the mud presence in the system remains comparatively low. SLR results in muddier shoals with landward locations mainly experiencing the largest differences, while the mud content in the channels does not change much. A difference in the mud settling velocity (w_s) has an impact on the mud availability in

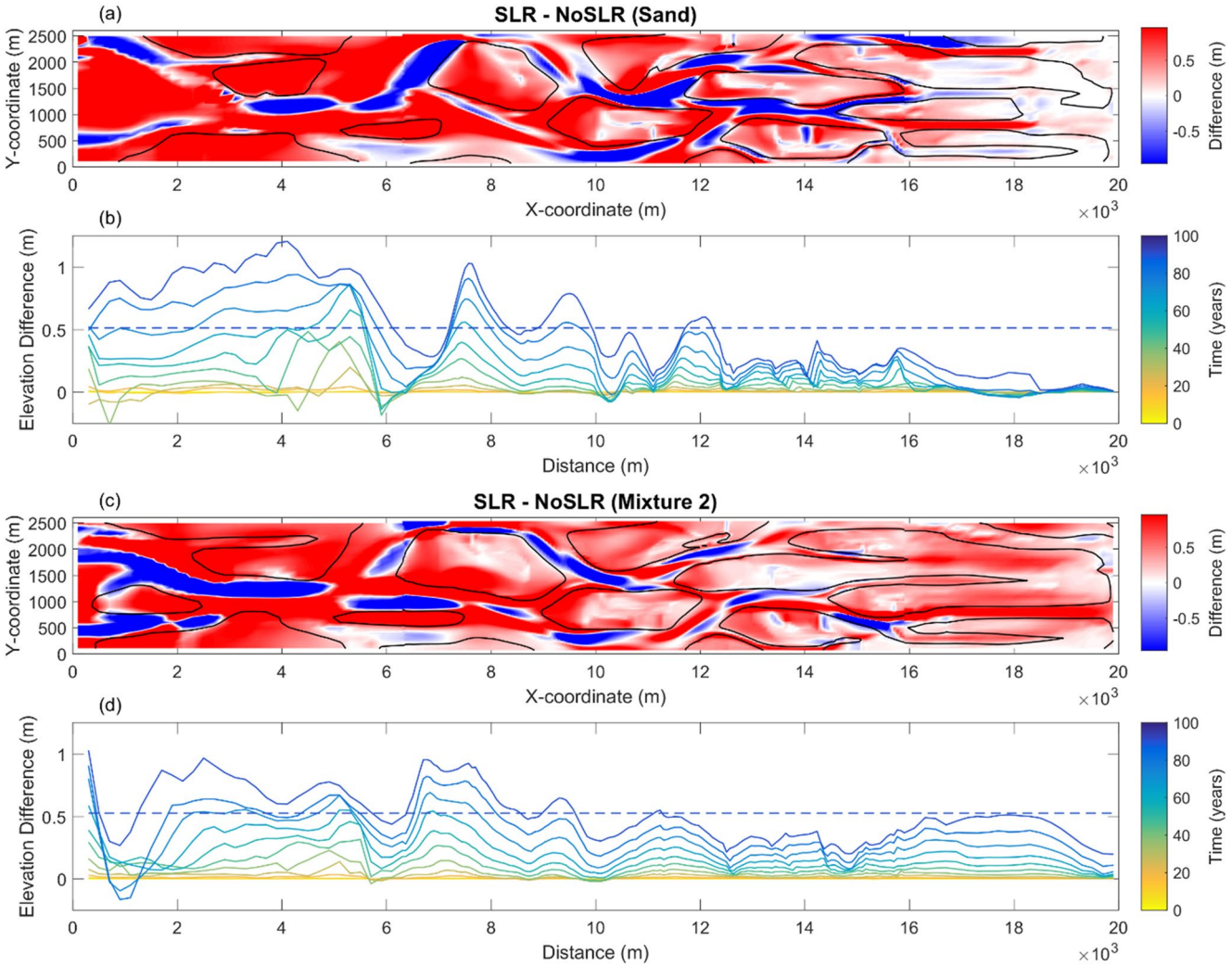

Figure 13. (a, and c) The elevation difference (m) between the SLR and No SLR scenarios for the sand (BW) and mixture 2 (Mix2) simulations, respectively. The black contour line indicates the border (LW) between the intertidal shoals and channels. (b, and d) The colored solid lines show the temporal development of the width averaged elevation difference. The dotted line shows the end elevation difference averaged over the whole domain.

the system. With the w_s of 1 mm/s (Mix2), mud is more easily deposited on the shoals which results in muddier shoals than the lower w_s of 0.5 mm/s (Mix1). However, the deposition locations are similar for both cases. Mud fractions favor deposition in locations subjected to low flow velocities and wave attack such as downwind shoal locations and landward shoals.

5. Discussion

In accordance with previous studies (e.g., Coeveld et al., 2003; Hibma, 2004; van der Wegen & Roelvink, 2008), this study shows that tide-residual sediment transports are the main driver of the morphological development of channel-shoal systems in a tidal embayment. Our work highlights that changes in the tidal currents combined with the sediment availability drive the SLR morphodynamic adaptation of intertidal sandy shoals by accretion. Wave action is a secondary but important process which impacts the shoal morphology but not the basin's SLR response. The presence of fine sediment supply (mud) enhances the morphological adaptation.

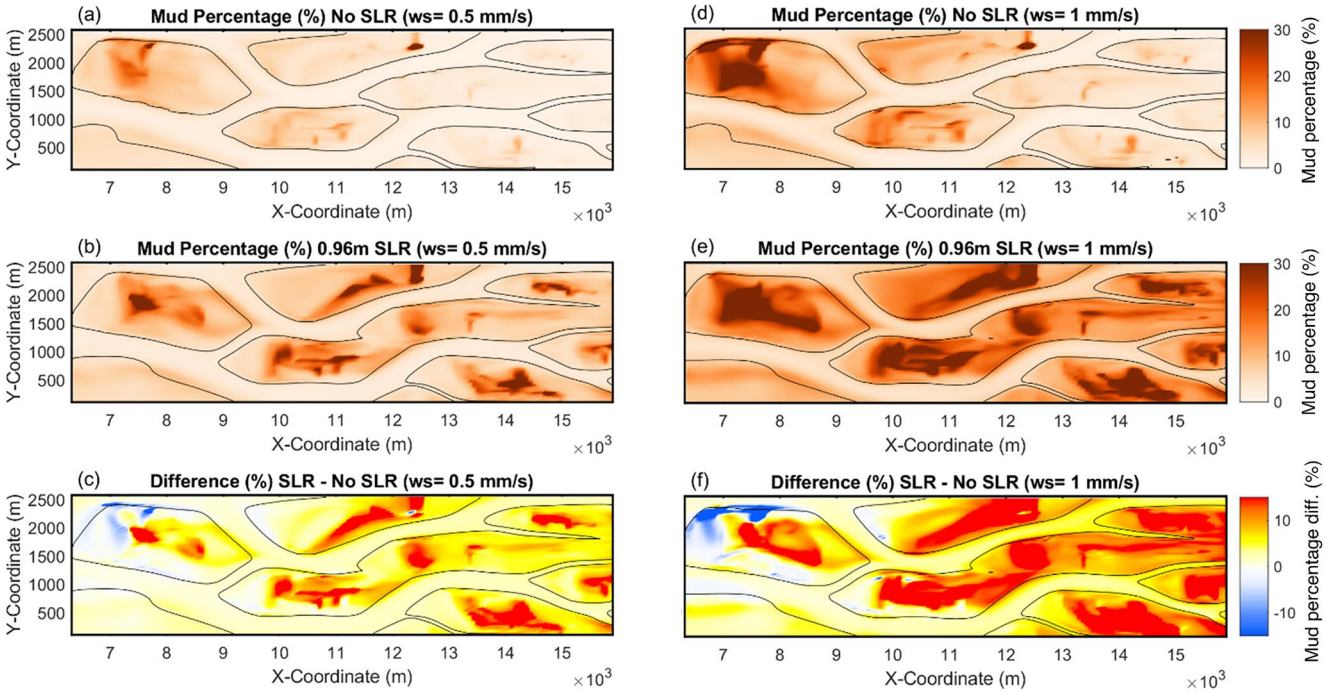

Figure 14. The mud percentage (%) in the top 0.25 m sediment layer for the simulation with a settling velocity of (a, and b) w_s = 0.5 mm/s, and (d, and e) w_s = 1 mm/s each without and with SLR, respectively. The difference between the mud percentage (%) for the No SLR and the 0.96 m non-linear SLR scenario for the different settling velocities. The black contour lines indicate the border (LW) between intertidal shoals and channels.

5.1. Implications for Real Case Studies

Forcing conditions vary in nature between the different systems depending on the local environment and hydraulic conditions. We expect the relevance of the mechanisms underlying SLR adaptation (e.g., tidal action, sediment supply, and wave action) to vary between the different systems as well. Mudflats in San Francisco Bay are projected to accrete with SLR mainly due to a drop in the wave-induced shear stresses at larger water depths which allow for mud deposition (Elmilady et al., 2019; Ganju & Schoellhamer, 2010; van der Wegen et al., 2017). A lack of sediment supply constrains shoal accretion causing a notable decline of the intertidal areas due to the morphodynamic adaptation time lag.

Forcing conditions at the Wadden Sea basins are closer to those described in this study. The Wadden Sea sandy shoals accrete under current SLR mainly due to a tide-driven sediment import to the system caused by the creation of accommodation space under SLR, while waves play a secondary role by inducing sediment resuspension over the shoals (Dissanayake et al., 2009; Elmilady et al., 2020; Wang et al., 2018). During the Holocene, over the past 7000 years, the Wadden Sea tidal basins reacted to SLR by shifting landward. SLR not only caused a vertical increase in accommodation space but also a landward expansion of the basin boundary. An apparently insufficient external sediment sand supply could not fill this increase, leading to substantial erosion and recession of the coastline of the bounding barrier islands. Hence, the whole system migrated landward. With the deceleration of the Holocene SLR, the basin partly filled in and coastal recession declined (see Beets & van der Spek, 2000, for details). The construction of dykes and partial reclamation of the tidal basins prevent a landward translation of the Wadden Sea under future accelerating SLR. The predicted accelerating SLR is expected to increase the flood dominance of the system and the associated sediment import (Dissanayake et al., 2009; Seiffert et al., 2014; Wachler et al., 2020). Lodder et al. (2019), Wang et al. (2018) and Van Goor et al. (2003) predict a lag in the morphological adaptation to SLR leading to loss of intertidal areas. Their work highlights a critical SLR rate at which sediment import can become insufficient for the basin bed levels to follow the SLR causing the system to drown. Even with ample sediment availability, this drowning can occur due to insufficient transport capacity through the inlet.

The following sub-sections discuss some of our main modeling approach assumptions and their potential implications for our understanding of the SLR impact.

5.1.1. Marine Transgression

We simulate a constrained system and the active build-up of existing intertidal shoals under SLR. Figures S1, S2, and S3 in the Supporting information S1 show examples of constrained systems in the Netherlands (Wadden Sea basins), Australia (Venus Bay), and New Zealand (Otago Harbour). In natural unconstrained systems, marine transgression (lateral expansion or landward migration) may also occur as a SLR adaptation mechanism (Allen,1990; Beets & van der Spek, 2000; Guo et al., 2021; Townend et al., 2021). In addition to the active shoal build-up, marine transgression will lead to "passive shoal formation" due to the drowning of the coastal plain causing dry land to shift from the supratidal realm into the intertidal realm. Guo et al. (2021) show the lateral expansion of a convergent system forming new tidal flats along its margins while existing inner intertidal shoals experience accretion in response to SLR.

5.1.2. Interacting Time Scales

We follow an approach that is based on isolating a century-scale SLR impact signal in a system with low morphological activity. In reality, the modeled morphological development could occur over a much longer time scale. Also, in real case studies, there could be other simultaneous and ongoing morphological adaptations with different time scales (decadal to geological) that could influence the SLR adaptation. Around the world, estuaries and tidal basins are subjected to dredging activities (Depreiter et al., 2013), land reclamation (MacKinnon et al., 2012), subsidence (Fokker et al., 2018), and changes in the tidal regime (Eelkema et al., 2013), varying riverine discharges, and sediment supply (Jaffe et al., 2007; Portela, 2006; B. Zhu et al., 2020). Also, other systems are still infilling and not in equilibrium (e.g., de Haas et al., 2018; van der Spek, 1994). This includes systems that were formed by the Holocene SLR and are still adapting to the decreasing SLR rates to their current levels (van der Spek & Beets, 1992). The past century's relatively low global SLR (≈0.2 m/century) makes it difficult to discriminate the SLR impact from other adaptations. Calibrating and validating long-term morphological models using observed historical evolution (e.g., bathymetries) is a challenging task that comprises notable uncertainties and does not necessarily guarantee the ability to capture the SLR contribution to the morphological evolution. Also, such historical data sets with sufficient frequency are extremely scarce. This makes the schematized approach presented by this study necessary for understanding the fundamental processes.

5.1.3. Sediment Fractions and Supply

In nature, tidal flats/shoals form in sediment-rich environments with sufficient fine-grained sediment supply (e.g., Friedrichs, 2011; Gao, 2019). Channel-shoal systems usually comprise a wide range of sediment fractions including coarse material which mainly exists in energetic deep sections (e.g., Wadden Sea; Postma (1957), and Figure S4 in the Supporting Information S1). In this research, we implement two sand fractions. The coarse fraction mainly exists in channels and plays an important role in stabilizing the channel-shoal patterns such as by controlling the channel deepening, while shoals are mainly composed of the finer fraction. The existence of the finer sand fraction played an important role in the shoal SLR adaptation as it constituted the majority of the SLR-induced sediment import to the system causing the shoal accretion. They were more easily suspended and transported to fill the accommodation space created by the SLR. On the other hand, simulations with a single coarse sand fraction (not presented) showed limited shoal adaptation due to low SSC levels and associated transports.

The imposed Base case SSC levels are based on typical conditions in the Wadden Sea (Postma, 1961, 1967, 1981). We assumed a constant sediment source at the boundary, while this might not be the case in reality if the morphological response of other elements (e.g., ebb-tidal delta) leads to a change in prevailing SSC. Some systems are predicted to face sediment supply shortages, while other systems could experience an increase in sediment supply (e.g., due to the erosion of other morphological elements). Our sand supply sensitivity showed that a sediment supply shortage/increase could limit/enhance the morphological adaption, respectively. Adding a finer mud fraction also enhanced the morphological adaptation.

5.2. Future Work

Gradually increasing the complexity of schematized models is of great value to better understand the potential SLR impact. Our research contributes by adding waves, mud, and high-resolution modeling along with focusing on the intertidal shoals. Several subjects remain for future exploration.

In our research, we mainly focus on a meso-tidal environment with a semi-diurnal tidal signal. Sensitivity analysis with tidal ranges, a lunar spring-neap tidal cycle, and a schematized mixed semi-diurnal tidal cycle showed the same trend of SLR morphological adaptation. We recommend performing a more detailed investigation of the impact of lunar and mixed semi-diurnal tidal cycles by testing different amplitudes and relative phasing. Also, overtides (e.g., M4, and M6) and their relative phasing could be highly relevant for the morphodynamics of tidal systems (e.g., Lesser, 2009). In addition, the impact of the SLR-induced changes of the tidal dynamics at the seaward boundary of tidal systems requires exploration.

We investigated non-convergent, short tidal basins which are dominated by intertidal shoals. Future work should investigate different geometries and bathymetries along with larger-scale basins and the availability of accommodation space. The dimensions (length, width, depth, and convergence) of tidal systems can impact their SLR adaptation (Leuven et al., 2019). Including riverine discharges and sediment supply makes findings more relevant to estuarine systems with notable riverine influence. Finally, implementing a more complex sand-mud interaction scheme would further increase the value of the results

6. Conclusions

Our work investigates the SLR impact on the long-term morphological development of intertidal sandy shoals. This includes exploring the importance of small wind-generated waves along with the mud presence to the intertidal morphodynamics. We implemented a 2DH process-based numerical model (D3D) which simulates the morphological evolution and the SLR adaptation of a channel-shoal system in a constrained short tidal basin dominated by intertidal shoals.

Tidal currents are the main driver of the channel-shoal system morphological evolution. Shoals evolve as a result of the tide-residual sediment transport convergence. Over time, the morphological activity gradually slows down as the residual transports diminish. Our work highlights that wave action is a secondary but important process which impacts the shoal morphology but does not fundamentally change the morphological evolution of the system. Wave-induced shear stresses enhance the sediment transport and distribution over shoals leading to lower and smoother intertidal flats.

Shoals accrete in response to SLR due to tide-residual sediment transports. Wave action, again, plays a secondary role in the sense that they impact the intertidal shoal morphology but not the basin's response to SLR in general terms. The morphodynamic adaptation lags behind SLR eventually leading to the drowning of intertidal shoal areas under SLR. Loss of shoal area favors flood dominance which**,** combined with the availability of sediment supply**,** triggers sediment import to the system. Locations near the sediment source experience more accretion both on a basin-scale and on a shoal-scale. A larger sediment supply enhances the SLR morphodynamic adaptation. Waves help distribute sediment supplied from channels across shoals. The presence of mud enhances the morphodynamic adaptation leading to faster, more uniform, accretion and muddier shoals under SLR.

The knowledge developed in this study serves as a fundamental step towards assessing the potential impact of SLR on the sustainability of valuable, intertidal environments. Future studies should focus on including other processes and forcing conditions.

Appendix A: Hydrodynamics

We apply the Delft3D (D3D) process-based numerical model (Deltares, 2017; Lesser et al., 2004). D3D-FLOW computes the flow by solving the unsteady two-dimensional shallow water equations (continuity and momentum). The continuity equation (Equation A1) and the horizontal momentum equations (Equations A2, and A3), neglecting the influence of density differences, and Coriolis force are as follows:

$$\frac{\partial \eta}{\partial t} + \frac{\partial hu}{\partial x} + \frac{\partial hv}{\partial y} = 0 \tag{A1}$$

$$\frac{\partial u}{\partial t} + u\frac{\partial u}{\partial x} + v\frac{\partial u}{\partial y} + g\frac{\partial \eta}{\partial x} + c_f \frac{u\sqrt{u^2+v^2}}{h} - v_e\left(\frac{\partial^2 u}{\partial x^2} + \frac{\partial^2 u}{\partial y^2}\right) - \frac{\tau_{sx}}{\rho h} - F_x = 0 \tag{A2}$$

$$\frac{\partial v}{\partial t} + v\frac{\partial v}{\partial y} + u\frac{\partial u}{\partial y} + g\frac{\partial \eta}{\partial y} + c_f\frac{v\sqrt{u^2+v^2}}{h} - v_e\left(\frac{\partial^2 v}{\partial x^2} + \frac{\partial^2 v}{\partial y^2}\right) - \frac{\tau_{sy}}{\rho h} - F_y = 0 \tag{A3}$$

with,

$$c_f = \frac{g}{c^2} \tag{A4}$$

where, η is the water level with respect to the datum, h is the water depth, u and v are the horizontal depth-averaged velocities in the x and y directions, respectively, g is the gravitational acceleration, ρ is the water density, c_f is the friction coefficient, c is the Chezy coefficient (60 $m^{1/2}/s$), v_e is the eddy viscosity (1 m^2/s), τ_s is the wind shear stress, and F_x and F_y are the depth-averaged wave-induced forcing.

Appendix B: Wave Model

The spectral wave Model SWAN (Booij et al., 1999; http://swanmodel.sourceforge.net/) is used in stationary mode to simulate the wind-generated waves. The SWAN model is based on the action density spectrum $N(\sigma,\theta)$, where σ is the relative frequency, and θ is the wave direction. The spectral action balance equation in Cartesian coordinates is:

$$\frac{\partial}{\partial t}N + \frac{\partial}{\partial x}c_x N + \frac{\partial}{\partial y}c_y N + \frac{\partial}{\partial \sigma}c_\sigma N + \frac{\partial}{\partial \theta}c_\theta N = \frac{S}{\sigma} \tag{B1}$$

where, c_x, c_y, c_σ, and c_θ are the propagation velocities in the x, y, σ, and θ-space, respectively. The first term on the left-hand side describes the local rate of change of the action density in time. The second and third terms describe the propagation of the action density in space. The fourth term describes the shift of the relative frequency due to depth and current variations. The fifth term describes the depth- and current-induced refraction. The right-hand side term denotes the source term for the action density which includes generation by wind, and dissipation by bottom friction, and depth-induced breaking. The D3D-Flow uses the gradients of the radiation stress tensor (S) to compute the depth-averaged wave-induced forcing (F_x and F_y; Equations B2 and B3) which is a source term in the momentum equations. Also, the hydrodynamic equations are solved in Generalised Lagrangian Mean (GLM; Andrews & Mcintyre, 1978) formulation in order to account for the stokes drift caused by the wave oscillating motion. Furthermore, the Fredsoe formulations (Fredsøe, 1984) are used to compute the maximum shear stress (τ_{max}) based on the combined current (τ_c) and wave (τ_w) shear stress.

$$F_x = -\frac{\partial S_{xx}}{\partial x} - \frac{\partial S_{yx}}{\partial y} \tag{B2}$$

$$F_y = -\frac{\partial S_{xy}}{\partial x} - \frac{\partial S_{yy}}{\partial y} \tag{B3}$$

Appendix C: Sediment Transport

Suspended sediment transport is calculated in the D3D by an advection-diffusion solver (Equation C1) which includes a sink and source term and is based on the local and time-varying velocities and water levels.

$$\frac{\partial hc}{\partial t} + \frac{\partial huc}{\partial x} + \frac{\partial hvc}{\partial y} = \frac{\partial}{\partial x}(h\varepsilon_h\frac{\partial c}{\partial x}) + \frac{\partial}{\partial y}(h\varepsilon_h\frac{\partial c}{\partial y}) + S \tag{C1}$$

where c is the sediment mass concentration (kg/m^3), ε_h is the prescribed horizontal diffusivity (7 m^2/s), S is the source/sink term which represents the exchange of sediment between the bed and flow (water column). The Van Rijn (1993) formulations are used to compute the sandy sediment transport for the combined effect of waves and currents for both bedload and suspended load transport. A reference height a is defined to distinguish between the bed and suspended transport as follows:

$$a = \min\left[\max\left(AKSFAC.k_s, \frac{\Delta r}{2}, 0.01h\right), 0.20h\right] \tag{C2}$$

where *AKSFaC* is a user-defined proportionality factor, k_s is a user-defined effective roughness height, Δr is the wave-induced ripple height (0.025 m). The critical bed shear stress is computed mainly based on the median sediment diameter (D_{50}) and according to the classical Shields curves. A reference concentration is calculated based on the sediment availability in the top bed layer (Van Rijn et al., 2000). This concentration is imposed at the reference height in order to entrain bed sediment to the water column. The settling velocity (w_s) of sand fractions in suspension is calculated based on (Van Rijn, 1993) as follows:

$$w_s = \frac{10\upsilon}{D_{50}}\left(\sqrt{1+\frac{0.01(s-1)gD_{50}}{\upsilon^2}}-1\right) \quad \text{for } 100\ \mu m < D_{50} \le 1000\ \mu m \tag{C3}$$

where, s is the relative density (ρ_s/ρ_w), and υ is the water kinematic viscosity coefficient. For more details on suspended sediment entrainment and deposition computation please refer to (Deltares, 2017). The bedload is calculated according to (Van Rijn, 1993) based on the combined flow and wave as follows:

$$|S_b| = 0.006\rho_s w_s D_{50}\frac{u_{\text{eff}}(u_{\text{eff}}-u_{\text{cr}})^{1.4}}{[(s-1)\text{gD}_{50}]^{1.2}} \tag{C4}$$

$$u_{\text{eff}} = \sqrt{u_R^2 + U_{\text{on}}^2} \tag{C5}$$

where, S_b is the bedload transport (kg/m/s), u_{eff} is the combined velocity magnitude (m/s) of the flow depth-averaged velocity and the near-bottom peak orbital velocity in the onshore direction based on the significant wave height (Hs), u_{cr} is the critical depth-averaged velocity for motion initiation based on Shields curve (m/s), u_R is the magnitude of an equivalent depth-averaged velocity (m/s), and U_{on} & U_{off} are the high frequency near-bed orbital velocities due to short waves in the on and offshore directions, respectively. The direction of the bedload transport is computed based on a division into current-induced transport ($S_{b,c}$) which acts in the flow direction and wave-induced transport ($S_{b,w}$) which acts in the wave direction.

$$S_{b,c} = \frac{S_b}{\sqrt{1+r^2+2|r|\cos\varphi}} \tag{C6}$$

$$|S_{b,w}| = r|S_{b,c}| \tag{C7}$$

$$r = \frac{(|U_{\text{on}}|-u_{\text{cr}})^3}{(|u_R|-u_{\text{cr}})^3} \tag{C8}$$

We apply the Partheniades-Krone formulations (Partheniades, 1965) for cohesive sediment transport as follows:

$$E = M\,S_e(\tau_{\text{cw}},\tau_{\text{cr},e}), \tag{C9}$$

$$D = w_s c_b S_d(\tau_{\text{cw}},\tau_{\text{cr},d}), \tag{C10}$$

where,

E	erosion flux (kg m^{-2} s^{-1})
M	erosion parameter (kg m^{-2} s^{-1})
$S_e(\tau_{\text{cw}},\tau_{\text{cr},e})$	erosion step function: $S_e(\tau_{\text{cw}},\tau_{\text{cr},e}) = (\frac{\tau_{\text{cw}}}{\tau_{\text{cr},e}}-1)$, when $\tau_{\text{cw}} > \tau_{\text{cr},e}$ $= 0$, when $\tau_{\text{cw}} \le \tau_{\text{cr},e}$
D	depositional flux (kg m^{-2} s^{-1})
w_s	sediment fall velocity (m/sec),
c_b	average near bottom sediment concentration,
$S_d(\tau_{\text{cw}},\tau_{\text{cr},d})$	deposition step function: $S_d(\tau_{\text{cw}},\tau_{\text{cr},d}) = (1-\frac{\tau_{\text{cw}}}{\tau_{\text{cr},d}})$, when $\tau_{\text{cw}} < \tau_{\text{cr},d}$ $= 0$, when $\tau_{\text{cw}} \ge \tau_{\text{cr},d}$

τ_{cw}	maximum bed shear stress due to current and waves (N m^{-2})
$\tau_{cr,e}$	critical erosion shear stress (N m^{-2})
$\tau_{cr,d}$	critical deposition shear stress (N m^{-2})

Data Availability Statement

There is no restriction on the data used in this study, readers can download the numerical model configurations and results, and the Wadden Sea data online at https://doi.org/10.6084/m9.figshare.14174597.

Acknowledgments
The modeling work in this study was carried out on the Dutch national e-infrastructure with the support of SURF Cooperative. This research was funded by Deltares Research Funds. The authors highly appreciate the thoughtful comments by the three anonymous reviewers and the associate editor, which helped improve the manuscript.

References

Airoldi, L., & Beck, M. (2007). Loss, status and trends for coastal marine habitats of Europe. *Annual Review*, *45*, 345–405. https://doi.org/10.1201/9781420050943.ch7

Allen, J. R. L. (1990). The Severn Estuary in southwest Britain: Its retreat under marine transgression, and fine-sediment regime. *Sedimentary Geology*, *66*(1), 13–28. https://doi.org/10.1016/0037-0738(90)90003-C

Allen, J. R. L., & Duffy, M. J. (1998). Medium-term sedimentation on high intertidal mudflats and salt marshes in the Severn Estuary, SW Britain: The role of wind and tide. *Marine Geology*, *150*(1–4), 1–27. https://doi.org/10.1016/S0025-3227(98)00051-6

Andrews, D. G., & Mcintyre, M. E. (1978). An exact theory of nonlinear waves on a Lagrangian-mean flow. *Journal of Fluid Mechanics*, *89*(4), 609–646. https://doi.org/10.1017/S0022112078002773

Beets, D. J., & van der Spek, A. J. F. (2000). The Holocene evolution of the barrier and the back-barrier basins of Belgium and the Netherlands as a function of late Weichselian morphology, relative sea-level rise and sediment supply. *Netherlands Journal of Geosciences - Geologie En Mijnbouw*, *79*(1), 3–16. https://doi.org/10.1017/S0016774600021533

Best, Ü. S. N., Van der Wegen, M., Dijkstra, J., Willemsen, P. W. J. M., Borsje, B. W., & Roelvink, D. J. A. (2018). Do salt marshes survive sea level rise? Modelling wave action, morphodynamics and vegetation dynamics. *Environmental Modelling & Software*, *109*, 152–166. https://doi.org/10.1016/J.ENVSOFT.2018.08.004

Blum, M. D., & Roberts, H. H. (2009). Drowning of the Mississippi Delta due to insufficient sediment supply and global sea-level rise. *Nature Geoscience*, *2*(7), 488–491. https://doi.org/10.1038/ngeo553

Booij, N., Ris, R. C., & Holthuijsen, L. H. (1999). A third-generation wave model for coastal regions: 1. Model description and validation. *Journal of Geophysical Research*, *104*(C4), 7649–7666. https://doi.org/10.1029/98JC02622

Braat, L., van Kessel, T., Leuven, J., & Kleinhans, M. G. (2017). Effects of mud supply on large-scale estuary morphology and development over centuries to millennia. *Earth Surface Dynamics*, *5*(4), 617–652. https://doi.org/10.5194/esurf-5-617-2017

Brinkman, A. G., Ens, B. J., Kersting, K., Baptist, M., Vonk, M., Drent, J., et al. (2001). *Modelling the impact of climate change on the Wadden Sea ecosystems. Dutch national research programme on global air pollution and climate change. Report no.: 410200066*. National Institute of Public Health and the Environment.

Carniello, L., Defina, A., Fagherazzi, S., & D'Alpaos, L. (2005). A combined wind wave-tidal model for the Venice lagoon, Italy. *Journal of Geophysical Research*, *110*(4), F04007. https://doi.org/10.1029/2004JF000232

Christie, M. C., Dyer, K. R., & Turner, P. (1999). Sediment flux and bed level measurements from a macro tidal mudflat. *Estuarine, Coastal and Shelf Science*, *49*(5), 667–688. https://doi.org/10.1006/ecss.1999.0525

Church, J. A., Clark, P. U., Cazenave, A., Gregory, J. M., Jevrejeva, S., Levermann, A., & Unnikrishnan, A. S. (2013). Sea level change. In *Climate change 2013: The physical science basis. Contribution of working group I to the fifth assessment report of the intergovernmental panel on climate change*. (In T. F. Stocker, et al. (Eds.)) (pp. 1137–1216). Cambridge University Press.

Coeveld, E. M., Hibma, A., & Stive, M. J. F. (2003). Feedback mechanisms in channel-shoal formation. *Coastal sediments conference, st. Petersburg, FL, USA*. (on CD-ROM).

de Haas, T., Pierik, H. J., van der Spek, A. J. F., Cohen, K. M., van Maanen, B., & Kleinhans, M. G. (2018). Holocene evolution of tidal systems in The Netherlands: Effects of rivers, coastal boundary conditions, eco-engineering species, inherited relief and human interference. *Earth-Science Reviews*, *177*, 139–163. https://doi.org/10.1016/j.earscirev.2017.10.006

de Vet, L. (2020). *Intertidal flats in engineered estuaries: On the hydrodynamics, morphodynamics, and implications for ecology and system management* (PhD dissertation). TU Delft. https://doi.org/10.4233/uuid:2b392951-3781-4aed-b093-547c70cc581d

de Vet, L., Prooijen, B., & Wang, Z. B. (2017). The differences in morphological development between the intertidal flats of the Eastern and Western Scheldt. *Geomorphology*, *281*, 31–42. https://doi.org/10.1016/j.geomorph.2016.12.031

Deltares. (2017). *Delft3D-FLOW: Simulation of multi-dimensional hydrodynamic flows and transports phenomena, including sediments. User Manual, Version 3.15, Revision 45038*. Deltares.

Depreiter, D., Sas, M., Beirinckx, K., & Liek, G. J. (2013). Dredging works in the Western Scheldt to deepen the navigation channel and to create ecologically valuable areas: Status after 3 years of monitoring. *Proceedings WODCON XX—congress and exhibition: The art of dredging*.

Dissanayake, D. M. P. K. (2011). *Modelling morphological response of large tidal inlet systems to sea level rise: UNESCO-IHE* (PhD dissertation). CRC Press.

Dissanayake, D. M. P. K., Ranasinghe, R., & Roelvink, J. A. (2009). Effect of sea level rise in tidal inlet evolution: A numerical modelling approach. *Journal of Coastal Research*, 942–946. Retrieved from http://www.jstor.org/stable/25737925

Du, J., Shen, J., Zhang, Y. J., Ye, F., Liu, Z., Wang, Z., et al. (2018). Tidal response to sea-level rise in different types of Estuaries: The importance of length, bathymetry, and geometry. *Geophysical Research Letters*, *45*(1), 227–235. https://doi.org/10.1002/2017GL075963

Eelkema, M., Wang, Z. B., Hibma, A., & Stive, M. (2013). Morphological effects of the eastern scheldt storm surge barrier on the ebb-tidal delta. *Coastal Engineering Journal*, *55*, 1–26. https://doi.org/10.1142/S0578563413500101

Elmilady, H., van der Wegen, M., Roelvink, D., & Jaffe, B. E. (2019). Intertidal area disappears under sea level rise: 250 years of morphodynamic modeling in San Pablo Bay, California. *Journal of Geophysical Research: Earth Surface*, *124*(1), 38–59. https://doi.org/10.1029/2018JF004857

Elmilady, H., van der Wegen, M., Roelvink, D., & van der Spek, A. (2020). Morphodynamic evolution of a fringing sandy shoal: From tidal levees to sea level rise. *Journal of Geophysical Research: Earth Surface*, *125*(6), e2019JF005397. https://doi.org/10.1029/2019JF005397

Fagherazzi, S., Palermo, C., Rulli, M. C., Carniello, L., & Defina, A. (2007). Wind waves in shallow microtidal basins and the dynamic equilibrium of tidal flats. *Journal of Geophysical Research*, *112*(F2), F02024. https://doi.org/10.1029/2006JF000572

Fan, D., Li, C., Archer, A., & Wang, P. (2002). Temporal distribution of diastems in deposits of an open-coast tidal flat with high suspended sediment concentrations. *Sedimentary Geology*, *152*, 173–181. https://doi.org/10.1016/s0037-0738(02)00067-2

Fokker, P., Van Leijen, F., Orlic, B., Marel, H., & Hanssen, R. (2018). Subsidence in the Dutch Wadden sea. *Netherlands Journal of Geosciences*, *97*, 129–181. https://doi.org/10.1017/njg.2018.9

Fredsøe, J. (1984). Turbulent boundary layer in wave-current motion. *Journal of Hydraulic Engineering*, *110*(8), 1103–1120. https://doi.org/10.1061/(ASCE)0733-9429(1984)110:8(1103)

Friedrichs, C. (2011). Tidal flat morphodynamics. In *Treatise on Estuarine and Coastal Science* (Vol. 3, pp. 137–170). https://doi.org/10.1016/B978-0-12-374711-2.00307-7

Friedrichs, C., & Aubrey, D. G. (1996). Uniform bottom shear stress and equilibrium hyposometry of intertidal flats. *Mixing in Estuaries and Coastal Seas*, *50*, 405, 429. https://doi.org/10.1029/CE050p0405

Friedrichs, C., Aubrey, D. G., & Speer, P. E. (1990). Impacts of relative sea-level rise on evolution of shallow estuaries. In R. T. Cheng (Ed.), *Residual Currents and Long-Term Transport*. *Coastal and Estuarine Studies* (Vol. 38, 105–122). Springer-Verlag New York, Inc. https://doi.org/10.1007/978-1-4613-9061-9_9

Galbraith, H., Jones, R., Park, R., Clough, J., Herrod-Julius, S., Harrington, B., & Page, G. (2002). Global climate change and sea level rise: Potential losses of intertidal habitat for shorebirds. *Waterbirds*, *25*(2), 173–183. https://doi.org/10.1675/1524-4695(2002)025[0173:gccasl]2.0.co;2

Ganju, N. K., & Schoellhamer, D. H. (2010). Decadal-timescale estuarine geomorphic change under future scenarios of climate and sediment supply. *Estuaries and Coasts*, *33*(1), 15–29. https://doi.org/10.1007/s12237-009-9244-y

Gao, S. (2019). Chapter 10—Geomorphology and sedimentology of tidal flats. In G. M. E. Perillo, E. Wolanski, D. R. Cahoon, & C. S. B. T.-C. W. Hopkinson (Eds.) (pp. 359–381). Elsevier. https://doi.org/10.1016/B978-0-444-63893-9.00010-1

Guo, L., Xu, F., van der Wegen, M., Townend, I., Wang, Z. B., & He, Q. (2021). Morphodynamic adaptation of a tidal basin to centennial sea-level rise: The importance of lateral expansion. *Continental Shelf Research*, *226*, 104494. https://doi.org/10.1016/j.csr.2021.104494

Herrling, G., & Winter, C. (2015). Tidally- and wind-driven residual circulation at the multiple-inlet system East Frisian Wadden Sea. *Continental Shelf Research*, *106*, 45–59. https://doi.org/10.1016/j.csr.2015.06.001

Hibma, A. (2004). *Morphodynamic modeling of estuarine channel-shoal systems*. (Ph.D dissertation). Technical University Delft. Retrieved from https://repository.tudelft.nl/islandora/object/uuid%3Af99c575b-b76b-4aa7-851d-0dca3d380759

Houser, C., & Hill, P. (2010). Wave attenuation across an intertidal sand flat: Implications for mudflat development. *Journal of Coastal Research*, *263*, 403–411. https://doi.org/10.2112/08-1117.1

Ikeda, S. (1982). Lateral bed load transport on side slopes. *Journal of the Hydraulics Division*, *108*(11), 1369–1373. https://doi.org/10.1061/JYCEAJ.0005937

Jaffe, B. E., Smith, R. E., & Foxgrover, A. C. (2007). Anthropogenic influence on sedimentation and intertidal mudflat change in San Pablo Bay, California: 1856-1983. *Estuarine, Coastal and Shelf Science*, *73*(1–2), 175–187. https://doi.org/10.1016/j.ecss.2007.02.017

Janssen-Stelder, B. (2000). The effect of different hydrodynamic conditions on the morphodynamics of a tidal mudflat in the Dutch Wadden Sea. *Continental Shelf Research*, *20*, 1461–1478. https://doi.org/10.1016/S0278-4343(00)00032-7

Jiang, L., Gerkema, T., Idier, D., Slangen, A. B. A., & Soetaert, K. (2020). Effects of sea-level rise on tides and sediment dynamics in a Dutch tidal bay. *Ocean Science*, *16*(2), 307–321. https://doi.org/10.5194/os-16-307-2020

Kemp, A. C., Horton, B. P., Donnelly, J. P., Mann, M. E., Vermeer, M., & Rahmstorf, S. (2011). Climate related sea-level variations over the past two millennia. *Proceedings of the National Academy of Sciences*, *108*(27), 11017–11022. https://doi.org/10.1073/pnas.1015619108

KNMI. (2014). *KNMI'14: Climate change scenarios for the 21st century—A Netherlands perspective*. KNMI.

Kohsiek, L. H. M., Buist, H. J., Misdorp, R., Berg, J. H., Visser, J., & Visser, J. (1988). Sedimentary processes on a sandy shoal in a Mesotidal Estuary (Oosterschelde, The Netherlands). In *Tide-influenced sedimentary environments and facies* (pp. 201–214). https://doi.org/10.1007/978-94-015-7762-5_16

Kopp, R. E., Kemp, A. C., Bittermann, K., Horton, B. P., Donnelly, J. P., Gehrels, W. R., et al. (2016). Temperature-driven global sea-level variability in the Common Era. *Proceedings of the National Academy of Sciences of the United States of America*, *113*(11), E1434–E1441. https://doi.org/10.1073/pnas.1517056113

Kuijper, C., Steijn, R., Roelvink, D., & van der Kaaij, T., (2004). *Morphological modelling of the western Scheldt: Validation of DELFT3D*. Deltares. Retrieved from http://www.vliz.be/en/imis?refid=103886

Lai, S., Loke, L. H. L., Hilton, M. J., Bouma, T. J., & Todd, P. A. (2015). The effects of urbanisation on coastal habitats and the potential for ecological engineering: A Singapore case study. *Ocean & Coastal Management*, *103*, 78–85. https://doi.org/10.1016/j.ocecoaman.2014.11.006

Le Bars, D., Drijfhout, S., & de Vries, H. (2017). A high-end sea level rise probabilistic projection including rapid Antarctic ice sheet mass loss. *Environmental Research Letters*, *12*(4), 44013. https://doi.org/10.1088/1748-9326/aa6512

Lesser, G. R. (2009). *An approach to medium-term coastal morphological modelling. PhD Thesis. UNESCO-IHE & Delft Technical University, Delft, The Netherlands*. CRC Press/Balkema.

Lesser, G. R., Roelvink, D., van Kester, J. A. T. M., & Stelling, G. S. (2004). Development and validation of a three-dimensional morphological model. *Coastal Engineering*, *51*(8–9), 883–915. https://doi.org/10.1016/j.coastaleng.2004.07.014

Leuven, J., Pierik, H. J., van der Vegt, M., Bouma, T. J., & Kleinhans, M. G. (2019). Sea-level-rise-induced threats depend on the size of tide-influenced estuaries worldwide. *Nature Climate Change*, *9*(12), 986–992. https://doi.org/10.1038/s41558-019-0608-4

Lipcius, R. N., Seitz, R. D., Wennhage, H., Bergström, U., & Ysebaert, T. (2013). Ecological value of coastal habitats for commercially and ecologically important species. *ICES Journal of Marine Science*, *71*(3), 648–665. https://doi.org/10.1093/icesjms/fst152

Lodder, Q. J., Wang, Z. B., Elias, E. P. L., van der Spek, A. J. F., de Looff, H., & Townend, I. H. (2019). Future response of the Wadden sea tidal basins to relative sea-level rise—An aggregated modelling approach. *Water*, *11*, 2198. https://doi.org/10.3390/w11102198

Lovelock, C. E., Feller, I. C., Reef, R., Hickey, S., & Ball, M. C. (2017). Mangrove dieback during fluctuating sea levels. *Scientific Reports*, *7*(1), 1680. https://doi.org/10.1038/s41598-017-01927-6

Maan, D. C., van Prooijen, B. C., Zhu, Q., & Wang, Z. B. (2018). Morphodynamic feedback loops control stable fringing flats. *Journal of Geophysical Research: Earth Surface*, *123*(11), 2993–3012. https://doi.org/10.1029/2018JF004659

MacKinnon, J., Verkuil, Y. I., & Murray, N. (2012). *IUCN situation analysis on East and Southeast Asian intertidal habitats, with particular reference to the Yellow Sea (including the Bohai Sea)*. International Union for the Conservation of Nature (IUCN).

Miller, K. G., Kopp, R. E., Horton, B. P., Browning, J. V., & Kemp, A. C. (2013). A geological perspective on sea-level rise and its impacts along the U.S. mid-Atlantic coast. *Earth's Future*, *1*(1), 3–18. https://doi.org/10.1002/2013EF000135

Murray, N. J., Clemens, R. S., Phinn, S. R., Possingham, H. P., & Fuller, R. A. (2014). Tracking the rapid loss of tidal wetlands in the Yellow Sea. *Frontiers in Ecology and the Environment*, *12*(5), 267–272. https://doi.org/10.1890/130260

Murray, N. J., Phinn, S. R., DeWitt, M., Ferrari, R., Johnston, R., Lyons, M. B., et al. (2019). The global distribution and trajectory of tidal flats. *Nature*, *565*(7738), 222–225. https://doi.org/10.1038/s41586-018-0805-8

Narayan, S., Beck, M. W., Wilson, P., Thomas, C. J., Guerrero, A., Shepard, C. C., et al. (2017). The value of coastal wetlands for flood damage reduction in the Northeastern USA. *Scientific Reports*, *7*(1), 9463. https://doi.org/10.1038/s41598-017-09269-z

NASA. (2020). S*ea level*. Retrieved from https://climate.nasa.gov/vital-signs/sea-level/

Partheniades, E. (1965). Erosion and deposition of cohesive soils. *Journal of the Hydraulics Division*, *91*(1), 105–139. https://doi.org/10.1061/jyceaj.0001165

Passeri, D. L., Hagen, S. C., Medeiros, S. C., Bilskie, M. V., Alizad, K., & Wang, D. (2015). The dynamic effects of sea level rise on low-gradient coastal landscapes: A review. *Earth's Future*, *3*(6), 159–181. https://doi.org/10.1002/2015EF000298

Portela, L. I. (2006). Calculation of sediment delivery from the Guadiana Estuary to the coastal. *Journal of Coastal Research*, 1819–1823. Retrieved from http://www.jstor.org/stable/25743075

Postma, H. (1957). Size frequency distribution of sands in the Dutch Wadden Sea. *Extrait Des Archives Néerlandaises de Zoologie*, *12*(3), 319–349.

Postma, H. (1961). Transport and accumulation of suspended matter in the Dutch Wadden Sea. *Netherlands Journal of Sea Research*, *1*(1), 148–190. https://doi.org/10.1016/0077-7579(61)90004-7

Postma, H. (1967). Sediment transport and sedimentation in the estuarine environment. In G.H. Lauff (Ed.), *Estuaries* (pp. 158-179). American Association for Advancement of Science.

Postma, H. (1981). Exchange of materials between the North Sea and the Wadden Sea. *Marine Geology*, *40*(1), 199–213. https://doi.org/10.1016/0025-3227(81)90050-5

Reed, D., van Wesenbeeck, B., Herman, P. M. J., & Meselhe, E. (2018). Tidal flat-wetland systems as flood defenses: Understanding biogeomorphic controls. *Estuarine, Coastal and Shelf Science*, *213*, 269–282. Academic Press. https://doi.org/10.1016/j.ecss.2018.08.017

Reineck, H.-E., & Singh, I. B. (1980). Tidal flats BT—Depositional sedimentary environments: With reference to terrigenous clastics. In H.-E. Reineck, & I. B. Singh (Eds.), (pp. 430–456). Springer Berlin Heidelberg. https://doi.org/10.1007/978-3-642-81498-3_26

Ridderinkhof, W., de Swart, H. E., van der Vegt, M., & Hoekstra, P. (2016). Modeling the growth and migration of sandy shoals on ebb-tidal deltas. *Journal of Geophysical Research: Earth Surface*, *121*(7), 1351–1372. https://doi.org/10.1002/2016JF003823

Roberts, W., Le Hir, P., & Whitehouse, R. J. (2000). Investigation using simple mathematical models of the effect of tidal currents and waves on the profile shape of intertidal mudflats. *Continental Shelf Research*, *20*(10–11), 1079–1097. https://doi.org/10.1016/S0278-4343(00)00013-3

Roelvink, J. A. (2006). Coastal morphodynamic evolution techniques. *Coastal Engineering*, *53*(2–3), 277–287. https://doi.org/10.1016/j.coastaleng.2005.10.015

Rossington, K., & Spearman, J. (2009). Past and future evolution in the Thames Estuary. *Ocean Dynamics*, *59*, 709–718. https://doi.org/10.1007/s10236-009-0207-4

Schramkowski, G. P., Schuttelaars, H. M., & de Swart, H. E. (2002). The effect of geometry and bottom friction on local bed forms in a tidal embayment. *Continental Shelf Research*, *22*(11–13), 1821–1833. https://doi.org/10.1016/S0278-4343(02)00040-7

Seiffert, R., Büscher, A., & Hesser, F. (2014). Impact of sea level rise on estuarine hydrodynamics. In R. Lehfeldt, & R. Kopmann (Hg.) (Eds.), *ICHE 2014. Proceedings of the 11th international conference on hydroscience & engineering* (pp. 1059–1066). Bundesanstalt für Wasserbau. S.

Seminara, G., & Tubino, M. (2001). Sand bars in tidal channels. Part 1. Free bars. *Journal of Fluid Mechanics*, *440*, 49–74. https://doi.org/10.1017/S0022112001004748

Sherwood, C. R., & Creager, J. S. (1990). Sedimentary geology of the Columbia River Estuary. *Progress in Oceanography*, *25*(1), 15–79. https://doi.org/10.1016/0079-6611(90)90003-K

Song, S., Wu, Z., Wang, Y., Cao, Z., He, Z., & Su, Y. (2020). Mapping the rapid decline of the intertidal wetlands of China over the past half century based on remote sensing. *Frontiers of Earth Science*, *8*. https://doi.org/10.3389/feart.2020.00016

Sweet, W. V., Kopp, R. E., Weaver, C. P., Obeysekera, J., Horton, R. M., Thieler, E. R., & Zervas, C. (2017). *Global and regional sea level rise scenarios for the United States*. NOAA/NOS Center for Operational Oceanographic Products and Services.

Thatcher, M. L., & Harleman, D. R. F. (1972). Prediction of unsteady salinity intrusion in estuaries: mathematical model and user's manual (Report No. MITSG 72-21). Cambridge, Massachusetts: S. G. P. O. Massachusetts Institute of Technology & N. S. G. P. (U.S.). Retrieved from https://repository.library.noaa.gov/view/noaa/96

Townend, I., Zhou, Z., Guo, L., & Coco, G. (2021). A morphological investigation of marine transgression in estuaries. *Earth Surface Processes and Landforms*, *46*(3), 626–641. https://doi.org/10.1002/esp.5050

van der Spek, A. J. F. (1994). *Large-scale evolution of Holocene tidal basins in the Netherlands* (PhD dissertation). Universiteit Utrecht, Faculteit Aardwetenschappen.

van der Spek, A. J. F., & Beets, D. J. (1992). Mid-Holocene evolution of a tidal basin in the western Netherlands: A model for future changes in the northern Netherlands under conditions of accelerated sea-level rise? *Sedimentary Geology*, *80*(3), 185–197. https://doi.org/10.1016/0037-0738(92)90040-X

van der Wegen, M. (2013). Numerical modeling of the impact of sea level rise on tidal basin morphodynamics. *Journal of Geophysical Research: Earth Surface*, *118*(2), 447–460. https://doi.org/10.1002/jgrf.20034

van der Wegen, M., Jaffe, B., Foxgrover, A., & Roelvink, D. (2017). Mudflat morphodynamics and the impact of sea level rise in south San Francisco bay. *Estuaries and Coasts*, *40*(1), 37–49. https://doi.org/10.1007/s12237-016-0129-6

van der Wegen, M., & Roelvink, D. (2008). Long-term morphodynamic evolution of a tidal embayment using a two-dimensional, process-based model. *Journal of Geophysical Research*, *113*(3), 1–23. https://doi.org/10.1029/2006JC003983

van der Wegen, M., & Roelvink, D. (2012). Reproduction of estuarine bathymetry by means of a process-based model: Western Scheldt case study, the Netherlands. *Geomorphology*, *179*, 152–167. https://doi.org/10.1016/j.geomorph.2012.08.007

van der Wegen, M., Roelvink, J. A., & Jaffe, B. E. (2019). Morphodynamic resilience of intertidal mudflats on a seasonal time scale. *Journal of Geophysical Research: Oceans*, *124*(11), 8290–8308. https://doi.org/10.1029/2019jc015492

Van Goor, M. A., Zitman, T. J., Wang, Z. B., & Stive, M. J. F. (2003). Impact of sea-level rise on the morphological equilibrium state of tidal inlets. *Marine Geology*, *202*(3–4), 211–227. https://doi.org/10.1016/S0025-3227(03)00262-7

van Maanen, B., Coco, G., Bryan, K. R., & Friedrichs, C. T. (2013). Modeling the morphodynamic response of tidal embayments to sea-level rise. *Ocean Dynamics*, *63*(11), 1249–1262. https://doi.org/10.1007/s10236-013-0649-6

Van Rijn, L. C. (1993). *Principles of Sediment Transport in Rivers, Estuaries and Coastal Seas* (Vol. 1006). Aqua publications Amsterdam.

Van Rijn, L. C., Roelvink, J. A., & Horst, W. T. (2000). Approximation formulae for sand transport by currents and waves and implementation in DELFT-MOR. (Technical Report. Z3054.40, WL). Deltares.

Wachler, B., Seiffert, R., Rasquin, C., & Kösters, F. (2020). Tidal response to sea level rise and bathymetric changes in the German Wadden Sea. *Ocean Dynamics*, *70*(8), 1033–1052. https://doi.org/10.1007/s10236-020-01383-3

Wang, Z. B., Elias, E. P. L., van der Spek, A. J. F., & Lodder, Q. J. (2018). Sediment budget and morphological development of the Dutch Wadden Sea: Impact of accelerated sea-level rise and subsidence until 2100. *Netherlands Journal of Geosciences*, *97*(3), 183–214. https://doi.org/10.1017/njg.2018.8

Wang, Z. B., & Roelfzema, A. (2001). *Long-term morphological modelling for humber estuary with estmorf*. In G. Li, & Z. Wang (Eds.). Tsinghua University Press.

Wentworth, C. K. (1922). A Scale of grade and class terms for clastic sediments. *The Journal of Geology*, *30*(5), 377–392. https://doi.org/10.1086/622910

Wilson, M. A., Costanza, R., Boumans, R., & Liu, S. (2005). Integrated assessment and valuation of ecosystem goods and services provided by coastal systems. In *The intertidal ecosystem: The value of Ireland's shores* (pp. 1–24). Royal Irish Academy. Retrieved from http://hdl.handle.net/102.100.100/182918?index=1

Zhou, X., Zheng, J., Doong, D.-J., & Demirbilek, Z. (2013). Sea level rise along the East Asia and Chinese coasts and its role on the morphodynamic response of the Yangtze River Estuary. *Ocean Engineering*, *71*, 40–50. https://doi.org/10.1016/J.OCEANENG.2013.03.014

Zhou, Z., Ye, Q., & Coco, G. (2016). A one-dimensional biomorphodynamic model of tidal flats: Sediment sorting, marsh distribution, and carbon accumulation under sea level rise. *Advances in Water Resources*, *93*, 288–302. https://doi.org/10.1016/J.ADVWATRES.2015.10.011

Zhu, B., Li, Y., Yue, Y., Yang, Y., Liang, E., Zhang, C., & Borthwick, A. G. L. (2020). Alternate erosion and deposition in the Yangtze Estuary and the future change. *Journal of Geographical Sciences*, *30*(1), 145–163. https://doi.org/10.1007/s11442-020-1720-0

Zhu, Q., van Prooijen, B. C., Wang, Z. B., & Yang, S. L. (2017). Bed-level changes on intertidal wetland in response to waves and tides: A case study from the Yangtze River Delta. *Marine Geology*, *385*, 160–172. https://doi.org/10.1016/j.margeo.2017.01.003